Water Mass Transports and Pathways in the North Brazil-Equatorial Undercurrent Retroflection

Ignasi Vallès-Casanova[1] , Eugenio Fraile-Nuez[2] , Marta Martín-Rey[1,3,4] ,
Erik van Sebille[5] , Anna Cabré[1] , Anna Olivé-Abelló[1] , and Josep L. Pelegrí[1]

[1]Departament d'Oceanografia Física i Tecnològica, Institut de Ciències del Mar, CSIC, Unidad Asociada ULPGC-CSIC, Barcelona, Spain, [2]Centro Oceanográfico de Canarias, Instituto Español de Oceanografía, CSIC, Santa Cruz de Tenerife, Spain, [3]Instituto de Geociencias, UCM-CSIC, Madrid, Spain, [4]Departamento de Física de la Tierra y Astrofísica, Universidad Complutense de Madrid, Madrid, Spain, [5]Institute for Marine and Atmospheric Research, Utrecht University, Utrecht, The Netherlands

Abstract The equatorial retroflection of the North Brazil Current (NBC) into the Equatorial Undercurrent (EUC) and its posterior tropical recirculation is a major regulator for the returning limb of the Atlantic Meridional Overturning Circulation. Indeed, most surface and thermocline NBC waters retroflect at the equator all the way into the central and eastern Atlantic Ocean, before they recirculate back through the tropics to the western boundary. Here, we use cruise data in the western equatorial Atlantic during April 2010 and reanalysis time series for the equatorial and tropical waters in both hemispheres in order to explore the recirculation pathways and transport variability. During the 1998–2016 period, the annual-mean EUC transports 15.1 ± 1.3 Sv at 32°W, with 2.8 ± 0.4 Sv from the North Atlantic and 11.4 ± 1.3 Sv from the South Atlantic. At 32°W most of the total EUC transport comes from the western boundary retroflection south of 3°N (7.2 ± 0.9 Sv), a substantial fraction retroflects north of 3°N (5.6 ± 0.4 Sv), and the remaining flow (2.3 Sv) joins through the interior basin. The South Atlantic subtropical waters feed the EUC at all thermocline depths while the North Atlantic and South Atlantic tropical waters do so at the surface and upper-thermocline levels. The EUC transport at 32°W has a pronounced seasonality, with spring and fall maxima and a range of 8.8 Sv. The 18 yr of reanalysis data shows a weak yet significant correlation with an Atlantic Niño index, and also suggests an enhanced contribution from the South Atlantic tropical waters during 2008–2016 as compared with 1997–2007.

Plain Language Summary In the western margin of the tropical Atlantic Ocean, the North Brazil Current (NBC) carries warm and salty waters across the equator northward into the Caribbean Sea. However, an important fraction turns eastward in the equatorial region, retroflecting into the Equatorial Undercurrent (EUC). We find that indeed most of the NBC-EUC retroflection water comes from the tropical and subtropical South Atlantic Ocean, but we observe that the EUC is also fed by North Atlantic waters, mostly from the north-eastern tropical Atlantic. Remarkably, these northern and southern water sources follow different retroflection pathways at different latitudinal bands and density layers. Subtropical water from the South Atlantic is present in all density layers while other sources reach the EUC at shallower layers. We also observe that the water transport associated with the NBC-EUC retroflection changes along the year, with maxima in spring and fall. Further, from 2008 to 2016 the EUC has increased slightly, associated with a greater contribution of South Atlantic tropical waters. This interannual variability is a result of local and remote changes of the trade wind system of the tropical Atlantic combined with climatic modes of variability such as the Atlantic Niño.

1. Introduction

The cross-equatorial northward flow in the western tropical Atlantic Ocean is carried mainly by western boundary currents flowing at surface and intermediate levels: the North Brazil Current (NBC) and the North Brazil Undercurrent (NBUC), transporting from salty thermocline South Atlantic Central Waters to low-salinity Antarctic Intermediate Waters (AAIW; e.g., Bourles et al., 1999; da Silveira et al., 1994; Stramma et al., 1995; Figure 1). These western boundary currents not only drive an inter-hemispheric water transport, which is associated with the returning branch of the Atlantic Meridional Overturning Circulation (AMOC; Bower et al., 2019; Tuchen et al., 2022), but also distribute South Atlantic waters into the equatorial ocean through a complex system of zonal currents (Hüttl-Kabus & Böning, 2008; Rosell-Fieschi et al., 2015). This zonal distribution arises at several
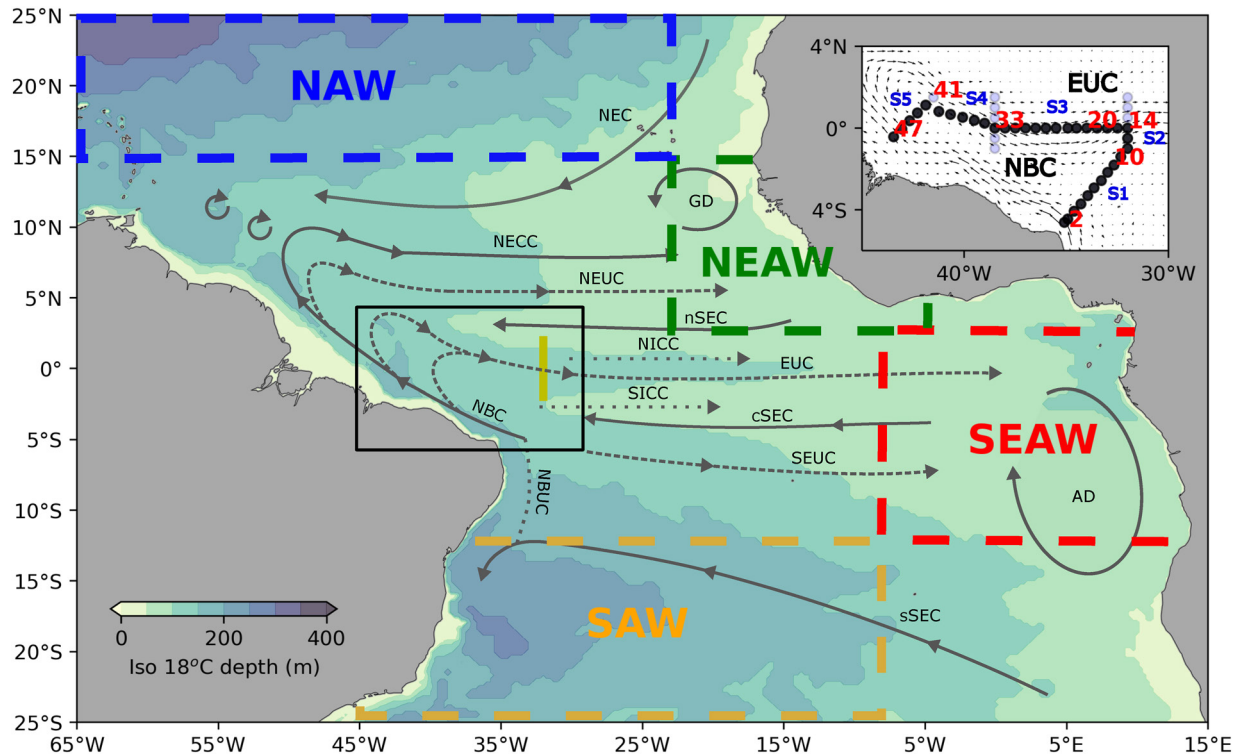
Figure 1. Schematics of the tropical Atlantic Ocean circulation system, overlaid onto the distribution of the 18°C isothermal depth in April 2010 from the GLORYS2v4 reanalysis. The main surface currents (continuous solid gray lines) are the North Equatorial Current (NEC), North Equatorial Countercurrent (NECC), and South Equatorial Current with northern, central, and southern branches (nSEC, cSEC, sSEC). At the thermocline layer (dashed black lines), we find the Equatorial Undercurrent (EUC) and its northern and southern counterparts (NEUC and SEUC). The South and North Intermediate Countercurrent (SICC and NICC) are also sketched (dotted lines). Northward western boundary currents are the North Brazil Current (NBC) and the North Brazil Undercurrent (NBUC). The Angola and Guinea domes (GD, AD) are outlined at the eastern margin. The MOC2 cruise area is delimited by the black rectangle that is displayed in the upper-right inset showing the locations of the hydrographic stations (dots), five referenced sections (labeled in blue) and the velocity vectors over the 18°C isothermal-surface as derived from the GLORYS2v4 reanalysis in April 2010; those stations that draw a closed box with the Brazilian coast are shown as black dots. The closed boxes in bold-dashed lines define the regions of different water sources that reach the 32°W section (yellow solid line), identified as North Atlantic Waters (NAW, dashed blue), Northeastern Atlantic Waters (NEAW, dashed green), Southeastern Atlantic Waters (SEAW, dashed red) and South Atlantic Waters (SAW, dashed orange).

locations along the western boundary pathway, with the northernmost position near 7°N−8°N, as the NBC turns east seasonally into the North Equatorial Counter Current (NECC), associated with the seasonal migration of the Intertropical Convergence Zone (ITCZ; Castellanos et al., 2015; Garzoli et al., 2004; Garzoli & Katz, 1983; Katz, 1987; Lumpkin & Garzoli, 2005; Polonsky & Artamonov, 1997; Rosell-Fieschi et al., 2015).

The NBUC feeds the eastward currents of the Equatorial Intermediate Current System located on both sides of the equator (Ascani et al., 2010). Similarly, within about 3°–4° north of the equator, the NBC upper-thermocline waters also turn eastward feeding a zonal system of equatorial near-surface currents. This system includes the Equatorial Undercurrent (EUC) along the equator and its northern and southern branches (NEUC and SEUC) at latitudes between 3° and 4°, north and south of the equator (Castellanos et al., 2015; Hüttl-Kabus & Böning, 2008; Lumpkin & Garzoli, 2005; Rosell-Fieschi et al., 2015; Schott et al., 2003, 2004; Stramma & Schott, 1999; Urbano et al., 2008; Figure 1).

The EUC is a permanent zonal current that carries salty and highly oxygenated waters across the entire equatorial Atlantic (Brandt et al., 2021), whose dynamics respond largely to the zonal wind-driven pressure gradient (Brandt et al., 2008; Metcalf et al., 1962; Stramma & Schott, 1999). The origin of the EUC was first described by Metcalf and Stalcup (1967), who concluded that the saltier and highly oxygenated EUC waters come mostly from the South Atlantic, with a minor contribution of North Atlantic Waters (NAW). Several Lagrangian studies have further assessed the contribution of the southern and northern masses to the EUC. Hazeleger et al. (2003), using a 1/4 degree resolution simulation with particles released along 20°W and traced backward in time, concluded

that the major EUC contribution comes from the tropical (southeast and central) South Atlantic, while less than 10% of the EUC waters come from the Northern Hemisphere, after subducting near the North Equatorial Current (NEC). White (2015) further confirmed that the EUC waters that upwell in the central equatorial region, in what constitutes the Atlantic cold tongue, originate at the western boundary of the subtropical South Atlantic through the NBUC.

The equatorial undercurrents (NEUC, EUC, and SEUC) combine with the tropical-subtropical overturning circulation in the upper-thermocline, known as the subtropical cells (STC), to ventilate the tropical basin: westward interior thermocline flow connects to the western boundary and recirculates east as the zonal undercurrent, drawing a gyre that includes upwelling at the equator and near-surface wind-driven poleward flow (Blanke et al., 1999; Hazeleger & Drijfhout, 2006; McCreary & Lu, 1994; Schott et al., 2004; Tuchen et al., 2019; Zhang et al., 2003). The complex interaction between this tropical recirculation and the net northward transport, which represents the returning limb of the AMOC, not only affects the heat and salt surface budget in the central and eastern equatorial upwelling regions (Claret et al., 2012; Jouanno et al., 2011; Kolodziejczyk et al., 2014; Schlundt et al., 2014) but also defines the exchange of mass and heat between both hemispheres and across the basin (Hazeleger & Drijfhout, 2006). In particular, Hazeleger and Drijfhout (2006) estimated that 6 Sv of AMOC waters are carried into the equatorial ocean by the EUC, with some 2 Sv recirculating back to the southern tropical hemisphere through the southern STC.

The temporal variability of the thermocline and the EUC is associated with ocean-atmosphere feedbacks of the tropical Atlantic climate system (Brandt et al., 2011, 2014, 2021; Foltz et al., 2019; Hormann & Brandt, 2009). The nonlinear contribution of remote and local forcing makes it difficult to identify the dominant mechanisms behind the EUC changes. Monitoring efforts (Bourlès et al., 2019, 2008; Johns et al., 2014) and model analyses (Arhan et al., 2006; Hazeleger et al., 2003; Hormann & Brandt, 2007; Philander & Pacanowski, 1986; Schott & Böning, 1991) indicate the presence of a semiannual cycle, with peak transports in boreal spring and a secondary fall maximum in the western margin. This seasonality has been recently associated with the presence of equatorial basin modes with semiannual and annual periods (Brandt et al., 2016). One challenge in establishing the EUC seasonality is that climate models generally underestimate the EUC intensity, as a consequence of biases in ocean stratification and wind stress (Richter & Tokinaga, 2020; Richter & Xie, 2008; Richter et al., 2012). Another main difficulty comes from the unresolved influence of the interannual tropical Atlantic variability (TAV), caused by the scarcity of long time series of in situ data covering the entire tropical basin (Foltz et al., 2019).

The main mode of interannual TAV during boreal summer, is associated with the development of anomalously high sea surface temperature (SST) in the eastern equatorial Atlantic associated with reduced trade winds, denoted as Atlantic Niño (Zebiak., 1993). The relation between EUC and Atlantic Niño has attracted the attention of the scientific community and is an active current line of research. The EUC is expected to strengthen during Atlantic Niña events and to weaken during Atlantic Niño (Brandt et al., 2014). Nevertheless, the diversity of Atlantic Niño events (Richter et al., 2013; Vallès-Casanova et al., 2020) together with the impact of local and remote forcing (Martín-Rey et al., 2018) hampers predicting the EUC interannual variability. In addition, fluctuations in EUC transport may be largely influenced by intense wave activity and tropical instabilities (Illig & Bachelery 2019; Illig et al., 2004; Perez et al., 2012; Polo et al., 2008; Tuchen et al., 2020; von Schuckmann et al., 2008).

Here, we provide new insights on the EUC origin through in-situ data and outputs from an ocean reanalysis, and present a detailed description of those waters reaching the westernmost EUC: water masses, mean transports and variability, and predominant pathways. The paper is organized as follows. The data and methodology are explained in Section 2. Section 3 presents observations taken during the oceanographic campaign MOC2, carried out in April 2010 along the western tropical Atlantic (red box, Figure 1). These data not only provide an Eulerian view of the velocity fields during the cruise but are also used to validate the model reanalysis. In Section 4, we offer the Lagrangian perspective, gauging the transports, pathways and transformations associated with waters from different sources (Sections 4.1 and 4.2) and assessing the spatiotemporal variations (Sections 4.3 through 4.5). Finally, Section 5 closes with the summary and main conclusions.

2. Data and Methods

2.1. Ship-Board Data

The MOC2 cruise was carried out onboard the R/V Hespérides in two legs, the first one taking place in the western boundary of the equatorial Atlantic Ocean between 7 and 18 April 2010 (Figure 1) and the second one representing a transoceanic section along 7°N between 20 April and 13 May 2010 (San Antolín Plaza et al., 2012; De La Fuente et al., 2014; Hernández-Guerra et al., 2014). In the first leg, a total of 47 hydrographic stations were occupied, sampling from the sea surface down to 1,500 m (or the seafloor if shallower; Figure 1; for a detailed view of the station coordinates see Figure S1 in Supporting Information S1; Claret et al., 2012). At each station, vertical casts of temperature, conductivity, and oxygen were obtained with a SeaBird 911-Plus multi-probe system mounted on a 24 Niskin-bottle rosette that collected water samples at standard depths, which were used to calibrate the conductivity and oxygen data (De La Fuente et al., 2014; Hernández-Guerra et al., 2014). The temperature and conductivity sensors were duplicated, as an additional measure for quality control. A closed box for the NBC retroflection region can be drawn using 36 out of the 47 field stations, which ends to the south-west with the Brazilian coastline (black dots in Figure 1 inner-panel). The EUC was also sampled until 1.5°N along the 32°W meridional section (stations 10–17) and between 1.0°S and 1.5°N along 38.5°W (stations 30–35).

Two lowered acoustic Doppler current profilers (LADCPs) were mounted on the rosette and deployed at each station. The LADCPs were RDI 300 kHz Workhorse Monitor instruments used in synchronized mode. The system was set to a ping-rate of 1 ping/s and a bin length of 10 m. An inverse method was applied for the post-processing of the raw data (IFM-GEOMAR LADCP software, Version 10.8, 7 February 2009; Visbeck, 2002). This resulted in high-quality velocity profiles, even in cases of very weak currents (<0.05 m s^{-1}). The LADCP velocity data were de-tided using the TPXO.3 global model of ocean tides (Egbert et al., 1994), and rotated to obtain the flow normal to the different segments of the box. Due to technical problems, LADCP profiles were not available at the first and last stations of the box (stations 1 and 47). As the depth at these stations was only about 200 m, data from a ship-mounted ADCP were used to fill these gaps.

A Monte Carlo method was applied to estimate the statistical uncertainty in mass transport for the entire box (Fraile-Nuez & Hernández-Guerra, 2006; Hammersley, 2013). The analysis is performed 2,000 times for the matrix u (u_i, i = 1, 2,000), simulated in the range $u - \delta u < u < u + \delta u$, where u is either velocity component as obtained from the LADCPs for each water depth and station and δu is the velocity uncertainty given by the LADCP software. With these new velocities, a sample of 2,000 mass transports is calculated and used to estimate the statistical uncertainty for each transect and layer.

2.2. Ocean Reanalysis Data

We use the three-dimensional fields of potential temperature (θ), salinity (S) and current velocity components (u, v, w) from the ocean reanalysis GLORYS2v4 (hereafter GLY), as provided by Mercator Ocean (Garric et al., 2017). The GLY reanalysis is obtained with the version 3.1 of the ocean NEMO model (Madec, 2008) that uses a tripolar ORCA grid with 0.25° horizontal resolution. The vertical grid has 75 levels, with 24 of them in the upper 100 m. The GLY reanalysis covers a time period of 23 yr, between 1993 and 2016, on a daily basis. The reanalysis assimilates along-track sea-level anomaly data, sea ice concentrations, SST and salinity profiles from the CORA4.1 in situ database (for further details, see von Schuckmann et al., 2017). Mignac et al. (2018) show that GLY represents the AMOC strength and meridional heat transport at 35°S better than other models and reanalyses.

We assess the model accuracy for our study region by comparing the modeled velocity, temperature, salinity, and density with the observations along the sampling sections during the MOC2 survey; throughout this article, whenever mentioning temperature and density, we will always implicitly refer to potential temperature and potential density. For this purpose, we use the daily outputs from GLY for the 14 days that the oceanographic survey lasted, extracting the modeled data at the locations of the hydrographic stations through linear interpolation; notice that these observations were not used in the model data-assimilation. Moreover, in order to ensure the reliability of GLY reanalysis on the upper equatorial circulation, the zonal velocities in the EUC core are compared with time series of observations as derived from the PIRATA subsurface mooring located at 23°W–0°N. The results are shown in the Supporting Information (Figures S3 and S4 in Supporting Information S1).

2.3. Lagrangian Approach

We exploit the three-dimensional GLY velocity with the Lagrangian framework OceanParcels (Delandmeter & van Sebille, 2019). OceanParcels is an off-line open-source tool for tracking particles in the ocean and inferring the predominant water-mass pathways. This Lagrangian tool uses a new interpolation scheme with the tracer computed as a constant value all over the cell, in accordance with the mass conservation schemes of C-grids (Delandmeter & van Sebille, 2019). In our simulations, since we are only interested in the average water mass pathways and not in tracer dispersion, particles are advected deterministically by the model velocity fields without adding sub-scale diffusion parameters.

In order to fully capture the retroflection waters that feed the EUC, we select the release section for our simulations along 32°W, between 2.5°S and 2.5°N. The vertical limits of the EUC are usually defined by the eastward flow taking place in thermocline layers with potential densities $24.5 < \sigma < 26.8$ kg m^{-3} (Brandt et al., 2006; Johns et al., 2014; Kolodziejczyk et al., 2009; Schott et al., 2005). Brandt et al. (2006) and Johns et al. (2014) have found that the EUC transport decreases from 20 Sv at 35°W to 14 Sv at 23°W, with most of the transport taking place in the upper ($24.5 < \sigma < 25.5$ kg m^{-3}) and lower thermocline ($25.5 < \sigma < 26.4$ kg m^{-3}) layers. At 35°W and 23°W, 5.4 and 3.0 Sv take place close to the surface ($\sigma < 24.5$ kg m^{-3}), respectively, while at 23°W only 1.1 Sv occurs in the deep-thermocline layer ($26.4 < \sigma < 26.8$ kg m^{-3}). Therefore, for our study, we define the EUC water parcels as those flowing east from the surface to the lower-thermocline layers, that is particles are released backward at each grid cell where the water flows eastward at the chosen time ($u_t > 0$) and $\sigma < 26.4$ kg m^{-3}.

The release section at 32°W is divided by cells of 0.25° latitudinal length and variable vertical length, equal to the vertical resolution of the reanalysis model. The particles are injected at each grid cell of the vertical section, its number proportional to the water transport through the cell. In this way, each seeded particle carries a fractional transport so that the sum of all particle transports amounts to the total water transport through the release section (Blanke et al., 1999). By tracking particles upstream or downstream, we obtain the horizontal streamlines for water parcels reaching or departing some geographical region—the Lagrangian stream functions (LSFs)—hence providing a view of the predominant water pathways. This can be safely done when 90% of the particles leave the model domain. In practice, the LSFs are derived by integrating the particle-transports along parallels, moving east from the western boundary and considering as positive (negative) counts those particles that move north (south), that is, particles always flow with larger LSF values to the right. For our LSF transport calculations, we count particles only the first time they cross a cell; in this way, we avoid overestimating the LSFs when virtual particles for exemple recirculate multiple times in the tropical gyre during the backtrack simulation.

The Lagrangian approach allows us to identify the relative contributions from the North and South Atlantic and to explore the possible exchange of tropical waters between both hemispheres. For this purpose, we classify the particles coming from three different water sources regions similar to the ones proposed by Urbano et al. (2008): South Atlantic Waters (SAW, [45°–8°W, 12°–25°S]), North Atlantic Waters (NAW, [65°–23°W, 15°–25°N]), and Northeastern Atlantic Waters (NEAW, [23°W, 3°–15°N]); additionally, we add a fourth region covering the Southeastern tropical Atlantic (SEAW, [8°W–12°E, 12°S–3°N]; boxes in Figure 1).

Similarly, we quantify transports of four different retroflection pathways that reach the EUC at different latitudes, between 3°S and 12°N. We classify the trajectories in three different latitudinal retroflection pathways: the south-equatorial retroflection (SER) refers to waters that turn east before reaching 0°S, the equatorial-retroflection (ER) relates to waters retroflecting between 0°S and 3°N, the north-equatorial retroflection (NER) identifies waters that turn eastward north from 3°N; and we also label particles that come directly from the North Atlantic Ocean in what we call northern-retroflection (NR). Notice that particles recirculating more than 4 yr in the retroflection area are excluded from the retroflection transports estimation.

The temperature and salinity values along the particle trajectories also come from the model, interpolated through the same C-interpolation scheme as the velocity components. Therefore, water mass transformations, including salt and heat fluxes, can be quantified as particles cross the temperature and salinity gradients.

We begin reporting on the MOC2 cruise. Thus, we first identify the source regions of different water mass sources and analyze their transformation as they reach the release section in April 2010. Further on, we expand our analysis for the entire GLY time span in order to capture the temporal variability of each water source.

3. Water Mass Transports During April 2010

3.1. Cruise Observations

We quantify the mass transports during the cruise through a combination of LADCP and hydrographic data. To this end, the water column is divided into surface plus upper-thermocline waters (essentially the STC waters, isopycnals with $\sigma < 26.4$ kg m^{-3}), mode waters (central waters of subtropical and subantarctic origin with potential densities between 26.4 and 27.1 kg m^{-3}) and intermediate waters (subantarctic waters with $27.1 < \sigma < 27.6$ kg m^{-3}; Figure 2). Vertical sections of potential temperature and salinity show a warm and salty layer, extending from about the sea surface down to about 200 m (Figures S2a and S2b in Supporting Information S1). This layer corresponds to salinity maximum water (SMW), which is formed by excess of evaporation over precipitation in the subtropics (Mémery et al., 2000). Below the SMW and down to about 400 m, we find the linear θ-S relationship that characterizes the central waters (Figure S4 in Supporting Information S1). AAIW occupies the 400–1,100 m layer, with potential temperature and salinity ranges of 4.5°C–10°C and 34.6–34.8 psu, respectively (Figures S2a and S2b in Supporting Information S1).

A northwestward penetration of the alongshore-flowing NBC takes place in the SMW and CW layers, between stations 1 and 4 (Figure 2a). The ADCP data show an intense boundary current (with velocities up to 1 m s^{-1}) in these two stations and within the layer from the sea surface to 27.1 kg m^{-3} that transports 14.4 ± 0.3 Sv into the box through the southwestern end and 16.6 ± 0.4 Sv out of the box through the northwestern end, in good agreement with estimates by Garzoli et al. (2004; 12.1 ± 2 Sv; near 3°N between the sea surface and 300 m) and Schott et al. (2005; 14.2 ± 2.4 Sv; near 5°S in the density range 24.5–26.8 kg m^{-3}). The 2.2 Sv transport increase between 5°S and 1°S is explained by surface inflow near the northwestern corner in excess of the NBC surface retroflection: a portion of this flow turns back clockwise toward the coast to rejoin the NBC, thereby supplementing the NBC transport. The main NBC retroflection continues eastwards as the EUC in the subsurface layer, meandering near the equator. The LADCP-inferred EUC transport leaving the box in the eastern margin, between stations 10 and 14, amounts to 9.5 ± 0.4 Sv; when accounting for the entire eastward flow along 32°W, that is stations 10–17 between 2°S and 1.5°N, the EUC transport increases to 15.4 ± 0.4 Sv.

In the intermediate layer, only the NBUC between stations 2 and 4 flows with the same northward orientation as the subsurface-central water (NBC). The NBUC penetrates into the box with a mean transport of 8.4 ± 0.3 Sv, in good agreement with earlier estimates of 8.9 ± 1.5 Sv by Schott et al. (2005). Moreover, this current has a salinity minimum of 34.45 psu, which is indicative of a purer source of AAIW (Figure S2b in Supporting Information S1). This undercurrent rapidly changes its orientation and flows southeastward out of the box through stations 4–10 into the South Intermediate Countercurrent (SICC), with an even larger mass transport: 11.4 ± 0.4 Sv. Between stations 10 and 14, just below the EUC, we observe a westward current into the box, with a transport of 6 ± 0.5 Sv. This subsurface westward flow splits into three branches. The first branch transports about 3 Sv southeastward, feeding the retroflection of the EIC into the SEUC and explaining its increase as compared with the NBUC. The second branch drives 1.3 Sv northward across the equator and the third branch continues northwestward with about 1.7 Sv, apparently into the North Intermediate Countercurrent (NICC).

The NICC exits the reference box in the intermediate layer between stations 38 and 41 with 10.4 ± 0.7 Sv, seemingly fed by the combination of the above westward third branch, a southward flow between stations 27 and 33 (6.5 ± 0.7 Sv), and a western boundary contribution between stations 41 and 47 (2.3 ± 0.5 Sv). The net imbalance of the intermediate water layer is estimated to be -0.1 ± 0.5 Sv.

3.2. Model Validation

In this section, we validate the GLY outputs by using the cruise data. Specifically, we compare the hydrographic and ADCP data with the modeled current velocity, temperature, and salinity, interpolated linearly at the cast positions. Following the previous section, we determine the mass transport balance by integrating along the closed box for subsurface, central and intermediate layers (Figure 2c). The modeled values are in very good agreement with observations at the surface and thermocline layers (correlation coefficient $r = 0.85$) but are in moderate concordance in the central waters ($r = 0.28$) and fail in the intermediate waters ($r = -0.05$). Note that the cumulative transports along the closed box may aggregate errors of the model velocities, hence suggesting greater disagreement (Figure 2c) than the actual velocity fields (Figures 2a and 2b). An alternative validation
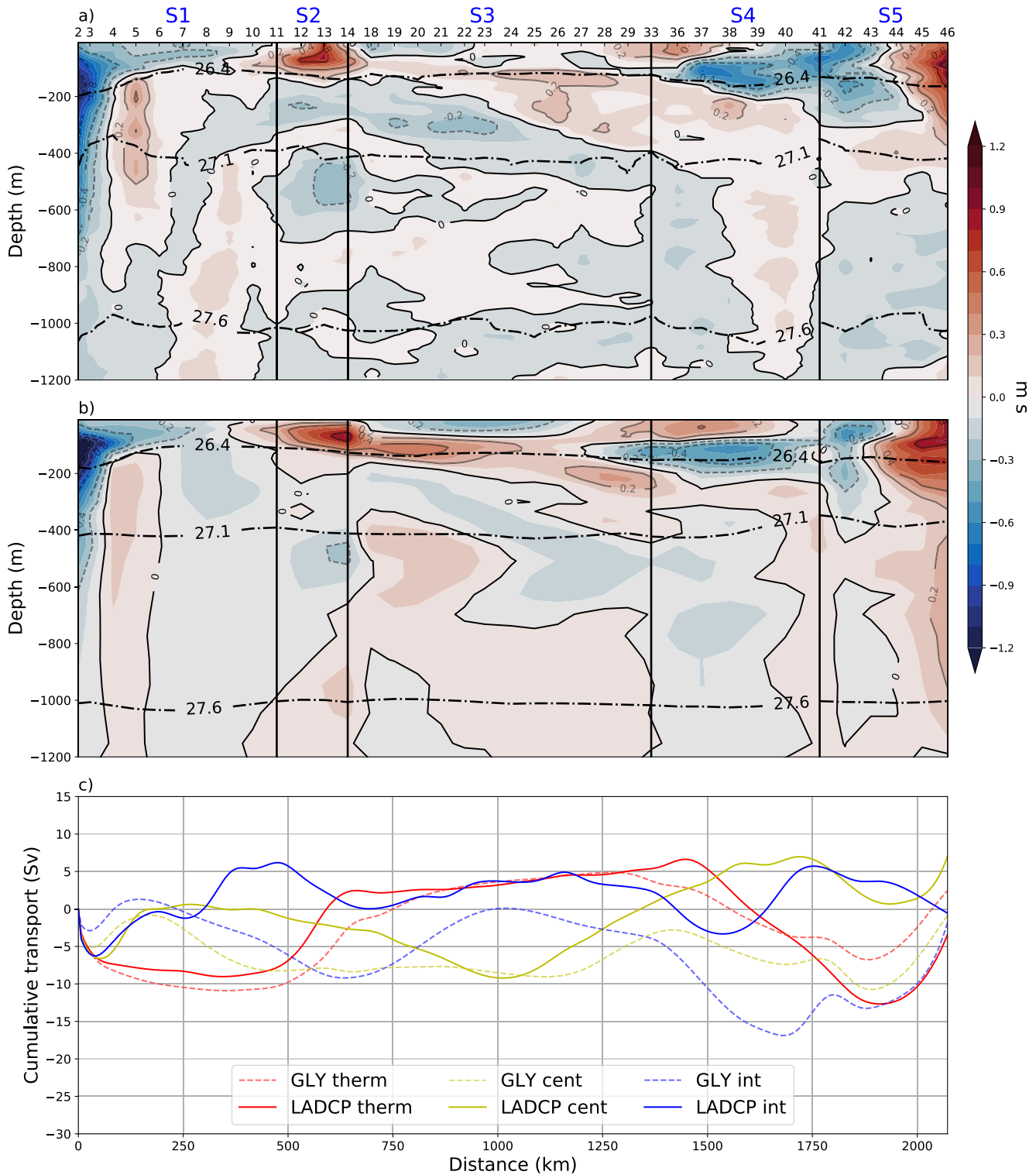
Figure 2. (a) Distribution of the normal-to section ADCP velocity, between the sea surface and 1,200 m, along the perimeter of the reference section in Figure 1, as if seen from outside the reference box; negative and positive values represent flow into and out of the reference box, respectively. The potential density surfaces 26.4, 27.1, and 27.6 kg m^{-3} are drawn as black dashed-dot contours. (b) Same as panel (a) but using the interpolated values from GLY. (c) Accumulated mass transport for the surface-thermocline (red), central (yellow), and intermediate (blue) waters; the solid lines represent the observed transports while the dashed lines are the transports as deduced from GLY. The vertical lines in all panels denote the limits of the S1 through S5 portions of the reference section, as shown in the inset of Figure 1.
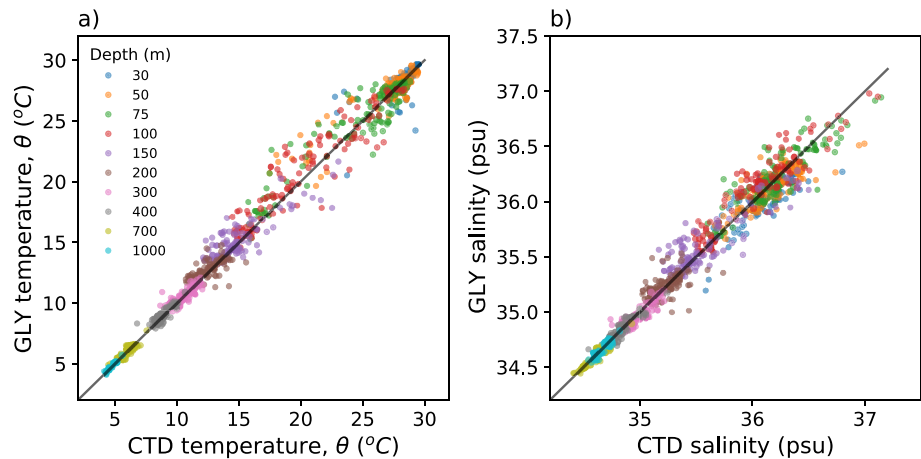
Figure 3. Scatter plots of in-situ observations versus the GLY reanalysis values interpolated at the stations: (a) potential temperature and (b) salinity. The variables are clustered by different depth levels (30, 50, 75, 100, 150, 200, 300, 400, 700, and 1,000 m), color-coded as indicated.

of the vertically integrated mass transports per unit length is found in the supplementary material (Figure S6 in Supporting Information S1).

The surface and thermocline flows are well captured by GLY (Figure 2b), with comparable NBC-EUC currents in the reanalysis and in the observations. Between stations 29 and 44, the EUC inflow differs moderately between observations and reanalysis. As the EUC outflows through the meridional section defined by stations 10–17, the core is weaker and located further north in GLY than in the observations, reflecting a less pronounced modeled EUC meander.

In the central waters, the model also underestimates the abrupt NBC southeast turn between stations 4 and 7 (Figure 2b). Further, the outflow between stations 36 and 42 is less intense and shifted north as compared with the observations. Within the intermediate layer, the flow differences are even more significant. This may be partly caused by the lower vertical resolution of the model with depth but likely reflects the substantial decrease of subsurface data that is assimilated in the reanalysis. The most remarkable difference is at the northwestern corner of the reference box, where the model shows that the NBUC outflows north while the observations indicate that the NBUC retroflects to feed the SICC and NICC. In general, the intermediate flow in GLY is not well captured as it is the case for most ocean models (Ascani et al., 2010; Ménesguen et al., 2019). Concretely GLY underestimates the retroflection into the SICC (stations 8–14) and the outflow of the NICC (it only appears in stations 40–41). Despite the differences, the integrated mass transports are close to zero for both model and observations (Figure 2c).

To evaluate the model accuracy in terms of temperature and salinity independently, we cluster the values at different depths and plot them against the observations (Figure 3; an alternative view is provided in Figure S5 in Supporting Information S1, which presents a salinity-temperature diagram for both observations and reanalysis). Overall, the model represents quite well the thermohaline structure of the study region. The maximum discrepancies are found in the subsurface and thermocline layers (50–150 m), which are also the regions of higher variability. At deeper levels (400–1,000 m), GLY also reproduces fairly well the temperature and salinity relationships.

In terms of temperature, the maximum mean difference appears at 100 m with 1.13°C and a standard deviation of 1.03°C (red dots, Figure 3a). With regard to salinity, the maximum mean difference is also found at 100 m with a value of 0.13 psu (red dots, Figure 3b), but the maximum standard deviation is found at 75 m with 0.09 psu (green dots, Figure 3b).

Despite the above-mentioned differences, the GLY reanalysis successfully captures the large-scale circulation patterns in the surface and thermocline layers. Time series of zonal velocity at 23°W–0°N from both the GLY model and the PIRATA observations show high correlation coefficients ($r > 0.6$) in the EUC core (Figures S3 and
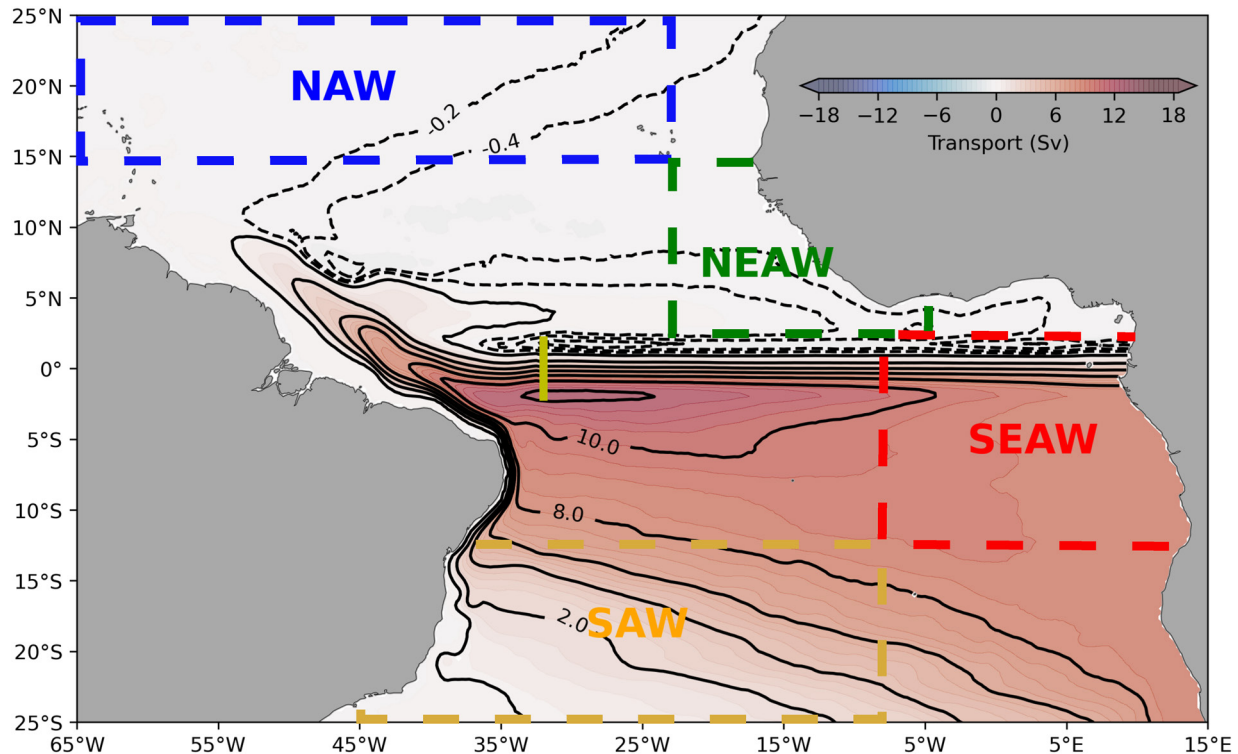
Figure 4. Lagrangian stream functions derived from particles released at the 32°W section (yellow solid line). Note the different negative and positive contours: while the former are dashed lines drawn every 0.2 Sv the latter are thick lines every 2 Sv. The closed boxes in bold-dashed lines define the regions of different water sources that ventilate the thermocline at the 32°W section: North Atlantic Waters (NAW, dashed blue), Northeastern Atlantic Waters (NEAW, dashed green), Southeastern Atlantic Waters (SEAW, dashed red) and South Atlantic Waters (SAW, dashed orange).

S4 in Supporting Information S1). We conclude that the model outputs provide us a useful tool to obtain a good characterization of the water mass sources and pathways into the EUC.

4. Sources and Pathways of the NBC-EUC Retroflection

4.1. Pathways and Water Mass Transformations

The LSFs summarize the main pathways feeding the EUC at 32°W during April 2010, nicely depicting the existence of an intense (weak) gyre in the South (North) Atlantic, and showing the arrival of waters all the way from the South Atlantic subtropical gyre (Figure 4). Note that for a proper computation of an LSF the flow should be non-divergent, which implies that we have to ensure that all particles start or end out of the domain (Blanke et al., 1999; Döös et al., 2008; Peña-Izquierdo et al., 2015). This is not possible when the release section is located near the middle of the basin, a requirement for studying the western equatorial retroflection, and causes a discontinuity of the stream functions at the eastern boundary (Figure 4).

Most of the EUC water sources are South Atlantic tropical and subtropical waters (Figure 4). Subtropical southern waters come via the southern branch of the South Equatorial Current (sSEC, see Figure 1), following the northern margin of the subtropical gyre. On the other hand, the recirculation of the tropical waters may follow either short or long routes. The short route takes place in the western and central Atlantic as a recirculation between the EUC and the central SEC (cSEC) at latitudes between 0° and 5°S (Figure 1); this is the region where the southern tropical cell (TC) occurs (Perez et al., 2014). The long path reaches the Gulf of Guinea, flowing south and turning westward at about 10°–15°S, joining with the sSEC subtropical waters. North of the equator, the EUC water comes mainly from the eastern tropical Atlantic. These eastern tropical waters are fed by the eastward NECC, turning westward to join the northern SEC (nSEC). There is also a small contribution of subtropical northern waters, originating at the NEC before joining in the NECC-nSEC-EUC connection (Figure 4).
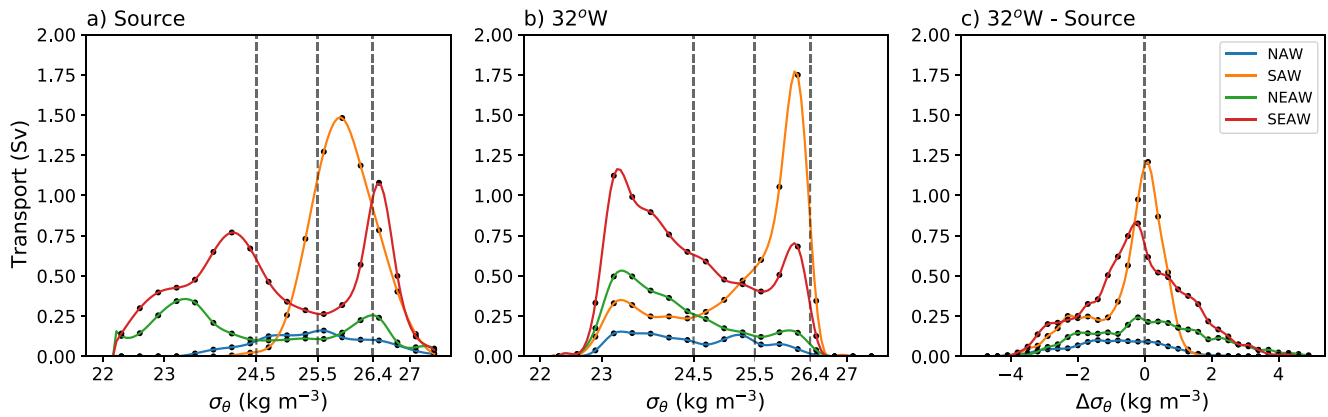
Figure 5. Lagrangian transports for 0.3 kg m^{-3} bins (a) at the source region and (b) at the release section; the dashed vertical lines define the lower limits of the surface, upper-thermocline, and lower-thermocline layers (24.5, 25.5, and 26.4 kg m^{-3}). (c) Transports for 0.3 kg m^{-3} bins as a function of the density change between the source region and release section; the vertical dashed line represents no density change and negative (positive) values indicate that waters at 32°W have become less (more) dense.

We investigate the contribution of the four source regions (SAW, SEAW, NAW, NEAW) to the EUC transport within the $22.0 < \sigma < 26.4$ kg m^{-3} density range, clustered in density bins of 0.3 kg m^{-3} (Figure 5). We start with the density distribution at origin (Figure 5a). The SEAW has a substantial contribution at all densities, with a major share in the surface layer ($\sigma < 24$ kg m^{-3}; Figure 5a). The SAW dominates in the lower-thermocline ($25.5 < \sigma < 26.4$ kg m^{-3}), which corresponds to SMW subducted in the subtropics. Most water originating from the NEAW is relatively fresh and warm Tropical Surface Water (TSW, $\sigma < 24.5$ kg m^{-3}), but there is some contribution from the lower-thermocline. North of 15°N the small contribution of NAW comes mostly from densities greater than 24.5 kg m^{-3} (Figure 5a).

Considering now the density distribution at the target section, we observe that the southern-origin waters dominate in all layers, with a predominance of SEAW and SAW in the surface and lower-thermocline layers, respectively. The NEAW appears as the next most pronounced surface contribution and the NAW is the less common one, although equally distributed in all layers (Figure 5b). In terms of density change $\Delta\sigma$, except for the NAW, all water sources have their maximum close to zero, indicating that most of the water-transport experiences no preferential net diapycnal transformation. The density-change distribution of the tropical waters is fairly symmetric but the subtropical waters have a net tendency to becoming lighter, with NAW having its main peak at $\Delta\sigma = -1$ kg m^{-3} and SAW having a secondary maximum near $\Delta\sigma = -2$ kg m^{-3} (Figure 5c). The source and 32°W transports are summarized in Table 1.

For a better understanding of the density changes, we visualize the Lagrangian transports from each source region in thermohaline coordinates (Figure 6). This picture helps identify the existence of diapycnal and isopycnal mixing, the latter displaying density-compensating changes in temperature and salinity (Döös et al., 2012; Tamsitt et al., 2018). Consistent with Figure 5c, the largest water transformations appear in the upper-thermocline layers of the NAW (Figure 6a) and the SAW (Figure 6c). These subtropical waters mix with the relatively warm

Table 1
Transport Contributions (Sv) to the EUC From the Different Source Regions, Classified in Different Potential Density Classes at the Initial (i) and Final (32°W) Locations

kg m^{-3}	SAW		SEAW		NAW		NEAW	
	i	32°W	*i*	32°W	*i*	32°W	*i*	32°W
$\sigma < 24.5$	0.04	1.59	4.19	4.98	0.24	0.71	2.04	2.32
$24.5 < \sigma < 25.5$	1.85	1.34	1.06	1.57	0.47	0.33	0.35	0.55
$25.5 < \sigma < 26.4$	3.69	3.42	1.71	1.45	0.34	0.16	0.60	0.37
$26.4 < \sigma < 26.8$	0.77	-	1.02	-	0.15	-	0.25	-
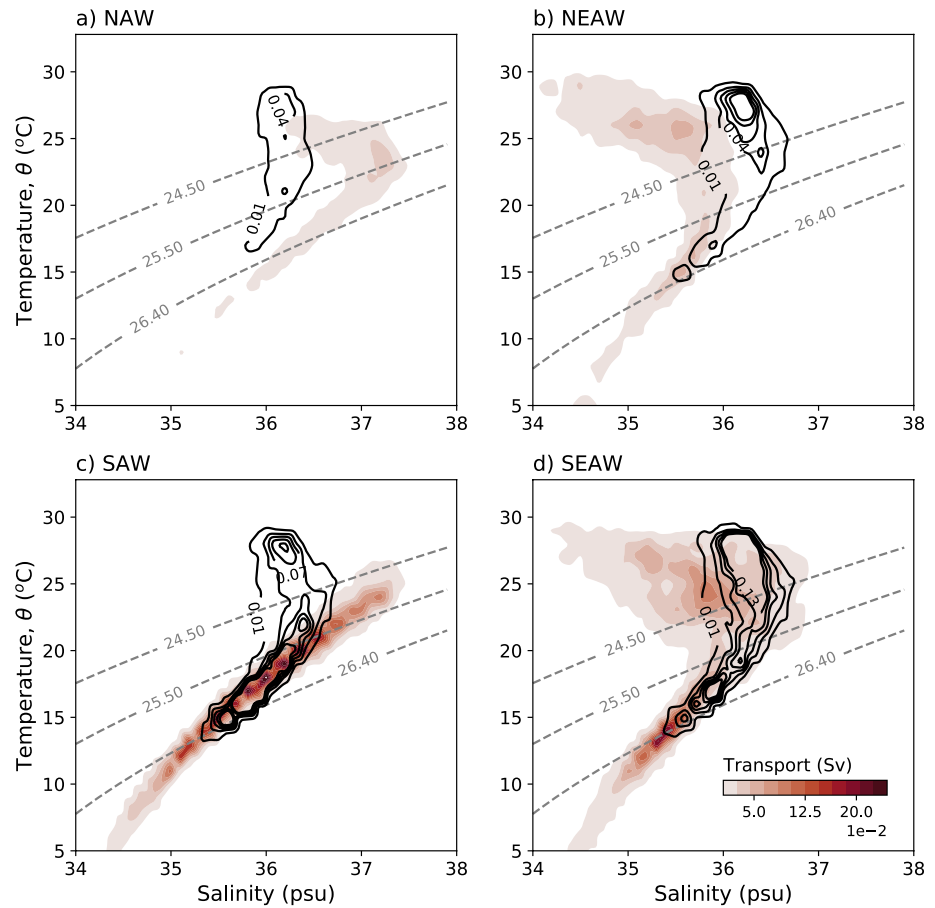
Figure 6. Transport in θ-S space, calculated for potential temperature and salinity bins of 0.2°C and 0.02 psu, respectively. Colors represent the distribution at the source locations, while solid contours refer to particles reaching the 32°W release section for (a) North Atlantic Water NAW, (b) Northeastern Atlantic Water NEAW, (c) South Atlantic Water SAW, and (d) Southeastern Atlantic Water SEAW. The dashed gray lines represent the lower isopycnals that delimit the surface, upper-thermocline, and lower-thermocline layers.

and fresh TSW (formed in regions of high insolation and where precipitation exceeds evaporation) and turn lighter during their course into the EUC.

In contrast, surface NEAW and SEAW get saltier and warmer as they reach the EUC (Figures 6c and 6d) but remain in the same density layer. Finally, in the lower thermocline the linear θ-S relationship in SAW and, to lesser extent, SEAW remains practically equal, showing similar transport values (Table 1).

4.2. Retroflection Pathways

Particles reaching the NBC retroflection zone turn eastward from the western boundary at different latitudes, between 3°S and 12°N, to feed the EUC at 32°W (Figure 7a, see Section 3.2). The SER refers to waters that turn east before reaching the equator, the ER relates to waters retroflecting between the equator and 3°N, the NER identifies waters that turn eastward north from 3°N, and NR denotes particles that come directly from the North Atlantic Ocean. The major retroflection corresponds to the NER, with 6.4 Sv in April 2010 that represent over 40% of the total EUC. At that time, the SER transport was 3.1 Sv while the ER was about 5.3 Sv, and the water turning from the North Atlantic accounted for 1.2 Sv.

The contribution of the different retroflection pathways reaching 32°W in April 2010 is shown in Figure 7c. The ER alone would produce a double EUC core (Figure 7d), with a peak value at about 60 m and a second maximum at about 80 m, but it is the NER that reinforces the deep core so as to produce the image of a single nucleus somehow stretching between the equator at about 60 m and 1°N around 90 m (Figure 7c). In contrast, the predominant
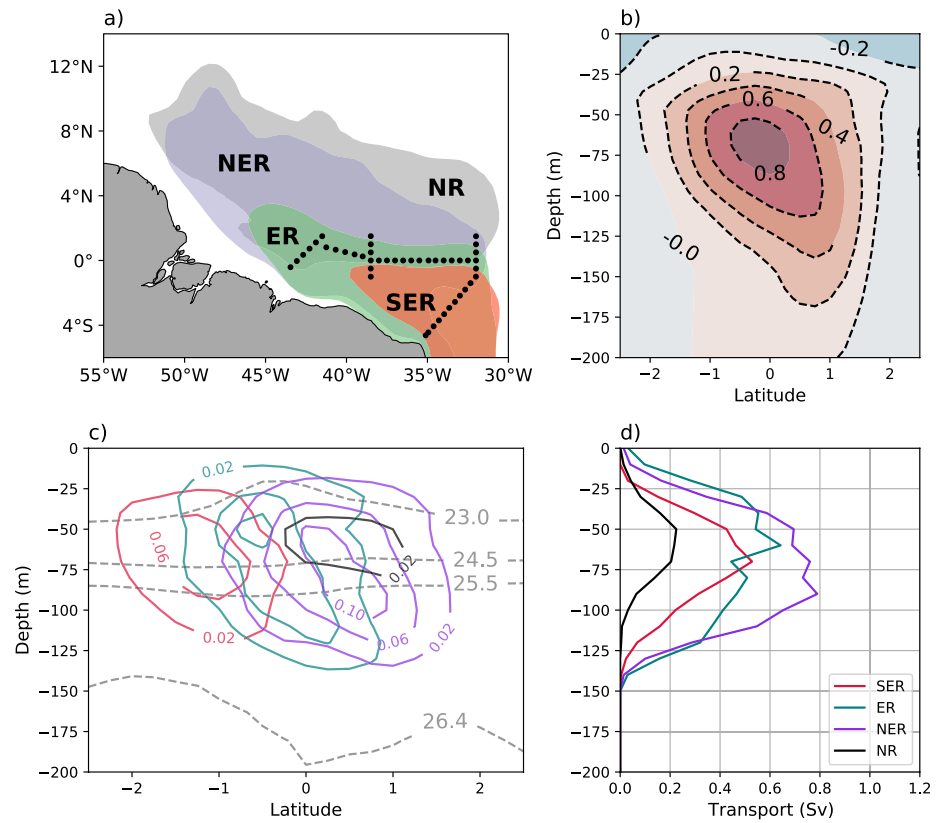
Figure 7. The NBC-EUC retroflection is divided into four main pathways relative to the equator: south-equatorial retroflection (SER, red color), equatorial-retroflection (ER, green color), north-equatorial retroflection (NER, violet color), and waters from the North Atlantic (NR, gray/black color). (a) Retroflection areas shaded by their respective colors, representing >75% of particles grouped per retroflection pathway. The black dots denote the locations of the hydrographic stations during the MOC2 cruise. (b) Latitude-depth distribution of zonal velocity at the 32°W section. (c) Latitude-depth transport distribution of the four pathways (solid-colored lines) plotted together with the density levels (gray-dashed contours); transports correspond to depth and latitude bins of 10 m and 0.25°, respectively. (d) Latitudinal-integrated transport in 10-m bins along 32°W for all retroflection pathways.

inflow from the SER and NR routes is located in the surface and upper-thermocline layers, between 60 and 80 m and changing in latitude between about 1°S (SER) and 0.7°N (NR; Figures 7b and 7c).

Figure 8 shows again the contribution of the several retroflection pathways at 32°W but now split among source regions. Southern waters (SAW and SEAW) are present in all retroflection routes that depart from the NBC (Figures 8c and 8d). The lower-thermocline waters from SAW dominate the deep core, at 0° for the ER and at 0.5°N for the NER, while the SEAW is associated with the shallow core between 1.5°S and 1.5°N, with ER and NER mainly contributing south and north of the equator (Figure 8d). The NAW and NEAW reach the shallow EUC core, with the NAW arriving along the NR and NER routes, and the NEAW including all NR, NER, and ER pathways (Figures 8a and 8c). Because of its latitudinal position, the NR appears closely tied to the NECC flow, looping through the interior basin of the tropical Atlantic and therefore dragging eastern waters through the nSEC (Figure 4).

4.3. Water Source and Pathway Variability

In the previous sections, we have focused our analysis on particles arriving at 32°W in April 2010, providing a Lagrangian perspective of the EUC observations during the MOC2 cruise. We may pursue the Lagrangian approach to explore the NBC-EUC pathways and transports during the entire GLY time series (1993–2016). For this objective, we take into account the travel times between the source regions and the 32°W release section, what is named the ramp-up period (van Sebille et al., 2014). These times are determined by comparing the
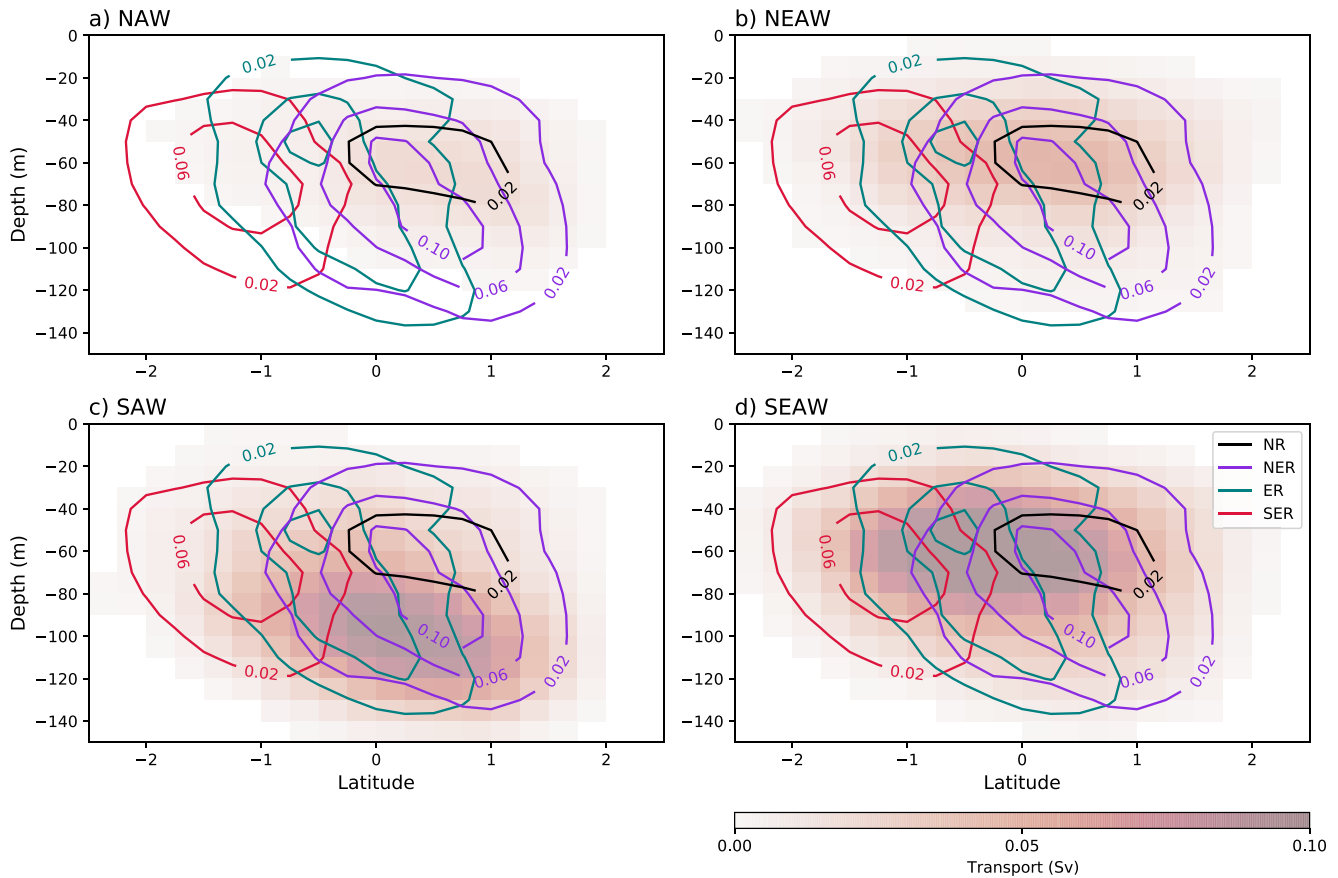
Figure 8. Latitude-depth transport distribution at section 32°W associated with each source region (shading): (a) North Atlantic Waters (NAW), (b) Northeastern Atlantic Waters (NEAW), (c) South Atlantic Waters (SAW), and (d) Southeastern Atlantic Waters (SEAW). Transports correspond to depth and latitude bins of 10 m and 0.25°, respectively. In order to illustrate the coincidence of source region and pathway, the contributions of the different equatorial pathways are overlaid: south-equatorial retroflection (SER, red line), equatorial retroflection (ER, green line), north-equatorial retroflection (NER, violet line) and North Atlantic retroflection (NR, black line).

time series of the Eulerian transport at the 32°W section with the Lagrangian transports from all source regions (Figure 9a). It turns out that, from 1997 onward, the sum of all Lagrangian transports is similar to the Eulerian transport with a correlation coefficient of 0.71 ($P < 0.05$). This happens earlier for the SAW than for the other sources, with a ramp-up of about 3 yr as compared with 4–5 yr. After removing these initial five years, the result is a time series of about 18 yr (1998–2016) that allows us to characterize the year-to-year transport variability (Figure 9).

The major contributions to the EUC transport come from the SAW and SEAW regions at all times (Figure 9b). From these two regions, the fraction of subtropical waters is higher than the tropical contribution until 2008. Remarkably, the SEAW contribution increases in 2008, becoming comparable to the SAW contribution (Figure 9). Similarly, the NEAW transport also experiences a slight increase in mean transport and variance from 2008 onwards (Figure 9b).

The transports associated with the different retroflection pathways are illustrated in Figure 9c. At first glance, by only considering the level of water transports, it would appear as if there might be a relation between water source and retroflection pathway as follows: NAW with NR, NEAW with SER, and the two southern waters (SAW and SEAW) with ER and NER. However, our previous analyses on the connection between source and pathway suggest that this relation will only hold for the northern subtropical waters (NAW) through the northern retroflection (NR). All other source waters (SAW, SEAW and NEAW) appear to weave in the NBC-EUC retroflection region, following all SER, ER, and NER pathways.
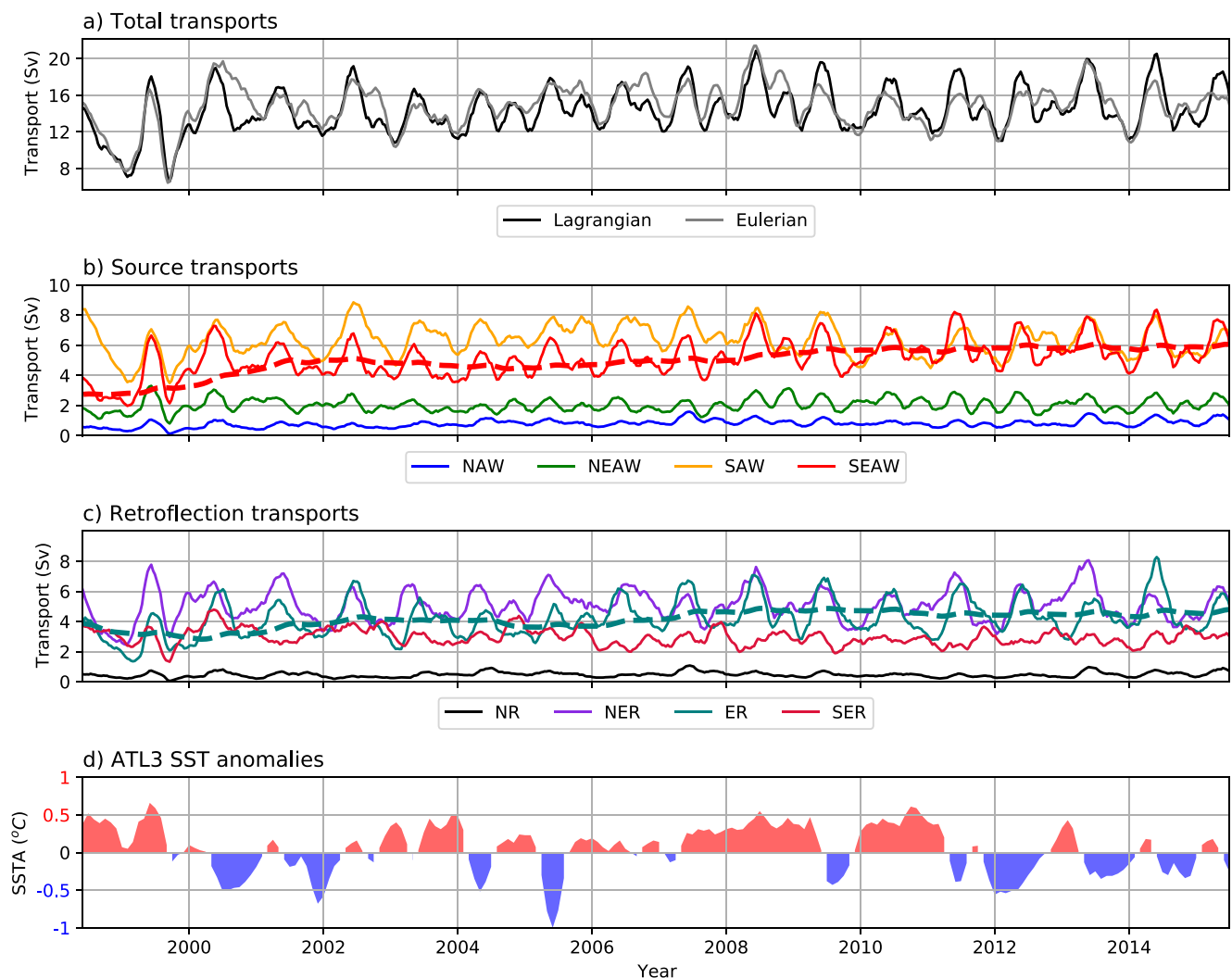
Figure 9. Time series of water transports, smoothed with a 6 month running-average. (a) Total Lagrangian (black line) and Eulerian (gray line) EUC transports at 32°W. (b) Lagrangian contributions from South Atlantic Waters (SAW, orange line), Southeastern Atlantic Waters (SEAW, red line), North Atlantic Waters (NAW, blue line), and Northeastern Atlantic Waters (NEAW, green line); the dashed red line is a 4-yr running average of SEAW transport. (c) Lagrangian transports for each retroflection pathway: south-equatorial retroflection (SER, red), equatorial retroflection (ER, green), north-equatorial retroflection (NER, violet), and north-retroflection (NR, black); the dashed green line is a 4-yr running average of ER transport. (d) ATL3 index monthly anomalies [20°W–0°, 3°N–3°S] as derived from the ERSSTv5 data set (Huang et al., 2017), following the criteria used in Vallès-Casanova et al. (2020).

Table 2 summarizes the annual mean and interannual variability in the partial and total transports at 32°W, both considering the water source and water pathway. The EUC Lagrangian transport is 14.3 ± 1.2 Sv and the EUC Eulerian transport is very similar, 15.1 ± 1.3 Sv. This slight difference is due to particles recirculating long time periods in the retroflection area, which are not accounted in any water source. The northern (NAW and NEAW) and southern (SAW and SEAW) source regions account for 2.8 ± 0.4 and 11.4 ± 1.3 Sv, respectively. The main retroflection pathway is NER (5.1 ± 0.4 Sv) followed by ER and SER. In 2010, the EUC Lagrangian transport

Table 2
Annual-Mean Values and Standard Deviations (in Sv) for the Eulerian and Total Lagrangian Transports at 32°W, the Latter Split in Source Regions (NAW, NEAW, SAW, SEAW) and Retroflection Pathways (NR, NER, ER, SER), for Both the 1998–2016 Period and for 2010

	Eulerian	Total	NAW	NEAW	SAW	SEAW	NR	NER	ER	SER
1998–2016	15.1 ± 1.3	14.3 ± 1.2	0.8 ± 0.2	2.0 ± 0.2	6.3 ± 0.5	5.1 ± 0.8	0.5 ± 0.1	5.1 ± 0.4	4.2 ± 0.6	3.0 ± 0.3
2010	14.7 ± 2.1	12.2 ± 2.9	0.7 ± 0.2	1.9 ± 0.7	5.0 ± 1.0	4.7 ± 1.4	0.4 ± 0.1	4.5 ± 0.8	3.3 ± 1.4	2.5 ± 0.4

Table 3
Correlations Between Source and Retroflection Equatorial Transports at 32°W, Calculated at Zero Time-Lag

	NR	NER	ER	SER
NAW	**0.89**	0.58	0.55	0.31
NEAW	0.48	**0.68**	0.52	0.46
SAW	0.46	**0.65**	**0.70**	0.39
SEAW	0.54	**0.74**	**0.69**	0.39

Note. Correlation values higher than 0.6 are shown in bold.

at 32°W is 2 Sv below the average, about half of this reduction arising from a decrease in the SAW source region and the ER pathway. At the time of the cruise, April 2010, the transport through 32°W was 15.4 Sv.

In order to identify if there is a preferential connection between origin and pathway, we have calculated the correlation at zero time-lag between the source and retroflection transports (Table 3). All correlations are significant ($P < 0.01$), indicating that the source variability translates out to all retroflection pathways. Considering only those correlations above 0.6, we can identify the following major connections: the NR accounts mostly for NAW, the NER accommodates northeastern (NEAW) and southern (SAW and SEAW) waters, and the ER is the dominant pathway for both southern waters (SAW and SEAW); in contrast, the SER shows the lowest correlation values (<0.5) with all water sources.

4.4. Interannual to Decadal Variability

At interannual time scales, the equatorial band is a key region for the emergence of the Atlantic Niño, which is the main mode of TAV (Zebiak, 1993). It peaks during boreal summer and is characterized by SST anomaly (SSTA) values covering the central-eastern equatorial Atlantic and extending along the African coast. The positive (negative) anomalous SSTs are associated with a weakening (strengthening) of the trade winds across the equatorial basin that trigger the propagation of equatorial oceanic waves (Lübbecke et al., 2010, 2018; Martín-Rey et al., 2019; Zebiak, 1993). The ATL3 index is a proxy of the Atlantic Niño, defined as the anomalous SST averaged in the region [3°S–3°N, 20°W–0°] (Figure 9d). ATL3 is negatively correlated with all Lagrangian transports at 32°W (statistical values from −0.12 to −0.17 for all water sources, always with $P < 0.1$), with time lags of either 1 month (SEAW, NAW, NEAW) or 2 months (SAW). This means that relatively warm conditions in the surface equatorial Atlantic are followed by a reduction of the equatorial transport 1–2 months later.

The negative correlation between equatorial SSTA and zonal transports is consistent with previous findings (Brandt et al., 2014; Hormann & Brandt, 2007). The low correlation scores can be understood in terms of the large diversity of TAV modes and their interaction with the background state (Martín-Rey et al., 2018; Vallès-Casanova et al., 2020). The emergence of the Atlantic Meridional Mode in boreal spring (Nobre & Shukla, 1996) and its potential connection with the Atlantic Niño via ocean waves (Foltz & McPhaden, 2010; Martín-Rey & Lazar, 2019) or meridional advection (Richter et al., 2013) provide an additional source of EUC variability. This diversity of mechanisms and responses has undoubtedly hampered the correct assessment of the linkage between TAV modes and EUC variability. In this context, an interaction between climatic modes and the variability of the NBC-EUC requires special attention in future studies.

Although the 1998–2016 time series is not long enough to evaluate multidecadal trends, the behavior of the EUC transport (Figure 9b) coincides with the reported strengthening of the Atlantic STCs during the last decade (Brandt et al., 2021; Tuchen et al., 2020). Besides the zonal pressure gradient, the EUC can be remotely forced by off-equatorial easterly winds and their associated Ekman poleward transports in both hemispheres, linked with the STCs. Brandt et al. (2021) bring to light a positive 10-yr trend in equatorial Ekman divergence during 2008–2018, which is associated with a strengthening of the northeast trade winds in the Northern Hemisphere. This intensification of the STC may lead to an increase of the SEAW and NEAW arriving to the EUC throughout the ER (Figures 9b and 9c).

4.5. The Seasonal Cycle

In order to analyze the seasonal cycle for each retroflection pathway and source region, we calculate the monthly Lagrangian transports for all transport time series (1998–2016) reaching the 32°W section, linearly detrend these time series and finally obtain the monthly averages (Figure 10). A semiannual cycle appears for the combined transport of all water sources, with a principal maximum in April (18.8 Sv), a secondary maximum in September, and minima in July and December (10.0 Sv; Figure 10a). When considering the different source contributions, we observe a rapid increase in water transport during boreal spring for all water sources, especially for the SAW and SEAW transports (Figure 10b).
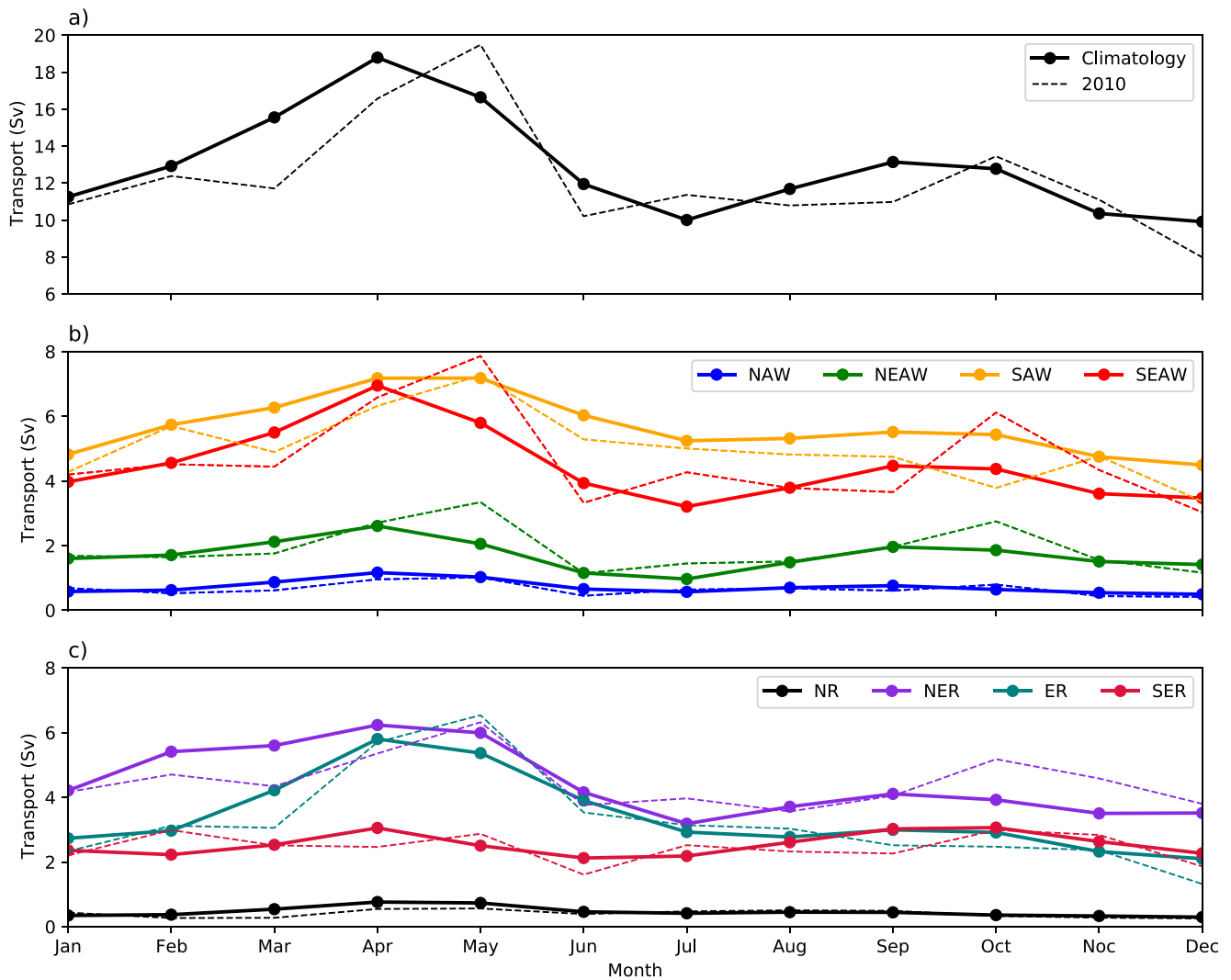
Figure 10. Monthly climatological transports at 32°W. (a) Total Lagrangian transports. (b) Transports split per source region: South Atlantic Waters (SAW, orange line), Southeastern Atlantic Waters (SEAW, red line), North Atlantic Waters (NAW, blue line), and Northeastern Atlantic Waters (NEAW, green line). (b) Transports split per equatorial pathway: south-equatorial retroflection (SER, red line), equatorial retroflection (ER, green line), north-equatorial retroflection (NER, violet line), and North Atlantic retroflection (NAR, black line). The solid lines in all panels correspond to monthly climatological transports, dashed lines to transports during 2010.

Regarding the seasonal contribution of each retroflection pathway, the most prominent feature is the difference between the equatorial (ER) and northern equatorial (NER) retroflections (Figure 10c). The NER reproduces the semiannual cycle while the ER has an annual cycle with a maximum in boreal spring and minimum in winter (Figure 10c). The secondary NER fall maximum is associated with the northward migration of the ITCZ: the south-easterlies in the northern equatorial region lead to the spring-fall westward development of the NECC, from the eastern Atlantic until connecting with the western boundary (Rosell-Fieschi et al., 2015). At this time, the latitudinal pressure gradient intensifies and leads to the NBC retroflection, raising an NEC-NECC cyclonic circulation (Figure 4). The eastward NECC waters eventually turn westward into the nSEC, having a significant yet relatively minor contribution to the surface and lower EUC thermocline layers ($\sigma < 26.4$ kg m^3).

The dominant spring maximum coincides with a season of reduced equatorial easterlies. Arhan et al. (2006) and Hazeleger et al. (2003) suggested that off-equatorial wind variations are driving this NBC-EUC spring supply. However, observations in the eastern equatorial Atlantic somehow differ from these western-basin results. Johns et al. (2014) reported that the main maximum occurs in boreal autumn at 23°W while a single boreal spring maximum was found at 0°E. They also found that at 23°W the transport remains quite high during boreal spring, being maximum at the upper and lower-thermocline levels, which is more alike with what we find at 32°W. Therefore,

this seasonal variability can be attributed to the resonance frequencies associated with equatorial basin modes, as suggested by Brandt et al. (2016). In their study, the semiannual and annual cycle of current velocities observed at 23°W are respectively attributed to the second and fourth baroclinic modes, respectively, excited by their resonance with the semiannual and annual wind forcing.

In 2010, despite the annual mean decrease of 2 Sv (Table 2), the bimodal transport pattern was reinforced (Figure 10a), associated with spring and autumn peaks (which lagged about one month after the mean values) and a decrease in the winter values. This took place mostly thanks to the contribution of both eastern tropical waters (SEAW and NEAW), while the SAW fall transport weakened (Figure 10b). When considering the retroflection pathways, the NER contribution was the principal cause for both the spring and autumn increases while the ER and NER inputs decreased during winter and early spring; the SER transports remain slightly below mean values for the entire year.

5. Discussion and Conclusions

The EUC is the principal conduit that diverts the western boundary NBC and recirculates the surface and upper-thermocline waters of the equatorial and tropical Atlantic Ocean. Thus, assessing the water mass contributions and pathways into the EUC is crucial not only to understand the dynamics of the equatorial and tropical oceans but also to predict the intensity and pathways of the AMOC returning limb. Recent observations depict the EUC as a crucial component of the AMOC return limb because it partly contributes to the zonally averaged upwelling within the upper layers (Tuchen et al., 2022). Previous studies have indeed demonstrated that most water that ventilates the equatorial thermocline through the NBC retroflection comes from the South Atlantic Ocean subduction region, where tropical and subtropical waters converge (Cabré et al., 2019). The different contributions from these southern sources, as well as waters originating in the North Atlantic, determine the composition of the surface and thermocline equatorial waters. In this study, we have examined the NBC-EUC retroflection system combining data obtained during an oceanographic cruise (MOC2 campaign in April 2010) and outputs from the ocean reanalysis GLORYS4v2. In particular, we have used reanalysis data through a combined Eulerian and Lagrangian approach.

The April 2010 Eulerian view, either observational or reanalysis, depicts an NBC that is largely retroflected at the equator into the EUC. The ADCP and reanalysis data show good agreement in the surface-thermocline ($\sigma < 26.4$ kg m^{-3}) and fair agreement in the central mode layers ($26.4 < \sigma < 27.1$ kg m^{-3}) but do less well in the intermediate layers ($27.1 < \sigma < 27.6$ kg m^{-3}). In particular, within the central layers the observed NBUC illustrates a large southward offshore flow that is not visible in the reanalysis. The cruise data down to 27.1 kg m^{-3} depict an NBC with 14.4 ± 0.3 Sv into the box and 16.6 ± 0.4 Sv out of the box. Most of this outflow feeds back into the EUC, with a transport of 15.4 ± 0.4 Sv at 32°W (9.5 ± 0.4 Sv taking place south of the equator).

In order to obtain the April 2010 Lagrangian perspective, we advected numerical particles with the three-dimensional velocity field of the GLORYS2v4 reanalysis. The Lagrangian transports allow us to quantify the water mass sources and pathways, as well as their transformations in density coordinates. We find that the predominant water contribution changes as we shift between density classes. The main water contribution to the EUC occurs within the lower-thermocline layer ($25.5 < \sigma < 26.4$ kg m^{-3}) led by the SAW. In contrast, the waters at the surface ($\sigma < 24.5$ kg m^{-3}) and upper-thermocline ($24.5 < \sigma < 25.5$ kg m^{-3}) layers are mainly from tropical sources, with SEAW as the dominant water mass followed by NEAW (Figure 5). Most of the SEAW remains at the surface, reaching the NBC-EUC retroflection via the cSEC; a portion of deeper SEAW moves southward along the eastern boundary (Mercier et al., 2003) and mixes back with warmer SAW, becoming lighter as it reaches the equator. SAW occupy the deeper layers at origin but lose density and upwell as they reach the equator. NAW and NEAW have smaller contributions, reaching the equatorial region through a south-eastward branch of the NECC that eventually feeds the westward nSEC toward the NBC-EUC retroflection (Figures 4 and 5).

Additionally, the modeled particle trajectories provide a complete picture of the April 2010 NBC-EUC retroflection pathways in the equatorial region. The dominant pathway is the NER (north of 3°N) followed by the ER (between the equator and 3°N), which feed all layers from the surface to the lower-thermocline (Figure 7). In contrast, the SER and NR pathways feed mainly the surface and upper-thermocline. The major contribution to the EUC lower-thermocline comes from the SAW via ER and NER, and the main inputs to the EUC upper thermocline and surface layers come from the SEAW via the ER-NER and from the NEAW via the NER (Figure 8).

The analysis of 18 yr of reanalysis data (1998–2016) shows that the spatiotemporal structure of the retroflection has high seasonal and moderate interannual variability. The Eulerian transports at 32°W, from 2.5°N to 2.5°S and above 26.4 kg m^{-3}, show that the annual-mean EUC is 15.1 ± 1.3 Sv, with 11.4 ± 1.3 Sv from the southeastern tropical (SEAW) and southwestern subtropical (SAW) waters and 2.8 ± 0.4 Sv from the northeastern tropical (NEAW) and northwestern subtropical (NAW). Western boundary waters retroflecting north of 3°N (NER) represent 5.1 ± 0.4 Sv while those diverting south of this latitude account for 7.2 ± 0.9 Sv.

At seasonal scales, we find a semiannual cycle in the EUC transport at 32°W, with a main peak in April and a secondary one in September and minima in July and December, in agreement with other model analyses (Arhan et al., 2006; Hazeleger et al., 2003; Hormann & Brandt, 2007) and observations (Johns et al., 2014). The monthly mean EUC transport varies between 10.0 Sv (July and September) and 18.8 Sv (April), a much greater range than interannual. The seasonal cycle has annual and semiannual periodicities, which result from the combination of the semiannual shallow NER and the annual ER (Figure 10). The autumn maximum, which is most prominent in the NER, is linked with the local oceanic linear-response to the equatorial trade winds (Rosell-Fieschi et al., 2015). Conversely, the ER shows a strong annual cycle with a spring maximum, which leads to a maximum SEAW contribution. These results are in good agreement with the horizontal pattern associated with equatorial basin modes, as derived from model data (Brandt et al., 2016).

All water sources are present in all the retroflection latitudinal pathways, revealing the semiannual cycle with a maximum transport in boreal spring. However, only the SEAW and NEAW, dominated by the NER, show a prominent fall maximum. Correlation values between transport time-series of retroflections pathways and water sources confirm the relation between origin and pathway found in 2010. NAWs are mostly advected by the NR. However, the NER is dominated by the tropical and subtropical South Atlantic Waters (SEAW and SAW), and the ER is highly correlated with the contribution of SEAW.

Additional seasonal-to-interannual transport fluctuations may originate from complex air-sea coupled interactions associated with the TAV modes (Brandt et al., 2014; Hormann & Brandt, 2007, 2009; Hormann et al., 2012). Nevertheless, the insufficiently long in-situ measurements and the diversity of spatiotemporal mechanisms have yet prevented from identifying direct cause-effect relations (Foltz et al., 2019; Martín-Rey et al., 2018; Vallès-Casanova et al., 2020). Our study does not have a detailed analysis of the interannual and decadal variability, yet we have noted a substantial transport increase of SEAW since 2008. Tuchen et al. (2020) show that an increase in the poleward Ekman transport, which results from an intensification of zonal wind stress in north tropical North Atlantic, has been compensated by westward surface flow from the central equatorial Atlantic since 2008. Mass conservation implies that this increase in the equatorial westward surface flows will lead to an increase in the EUC eastward transport. Indeed, our results suggest that the STC intensification drives an increase of tropical waters into the EUC.

Brandt et al. (2021) point out that the strengthening of the STC is probably linked with more intense trade winds in the northern hemisphere, associated with an emerging cold phase of the Atlantic Multidecadal Variability (AMV; Frajka-Williams et al., 2017), characterized by cold SSTA in the Tropical North Atlantic (TNA). In addition, variations in the AMV phase are associated with AMOC-induced subsurface thermocline adjustment in the TNA, where a warm (cold) AMV is associated with AMOC strengthening (weakening; Wang & Zhang, 2013). These relations may explain why the EUC intensification translates mostly into an increase of tropical waters from the South Atlantic (SEAW). Our results demand further research on the hypothetical linkage of the EUC with AMV, AMOC, and STC, which is relevant not only for resolving the variability in water properties carried by the EUC but particularly for assessing the different factors that control the efficiency of the AMOC returning limb.

Data Availability Statement

The hydrographic and biogeochemical cruise data is available at the Clivar and Carbon Hydrographic Data Office (Rios et al., 2012) and the hydrographic and velocity data for leg 1 of the cruise is available at Zenodo (https://doi.org/10.5281/zenodo.6359412; Pelegrí et al., 2022).

References

Arhan, M., Tréguier, A.-M., Bourlès, B., & Michel, S. (2006). Diagnosing the annual cycle of the Equatorial Undercurrent in the Atlantic Ocean from a general circulation model. *Journal of Physical Oceanography*, 36(8), 1502–1522. https://doi.org/10.1175/JPO2929.1

Ascani, F., Firing, E., Dutrieux, P., McCreary, J. P., & Ishida, A. (2010). Deep equatorial ocean circulation induced by a forced dissipated Yanai beam. *Journal of Physical Oceanography*, 40, 1118–1142. https://doi.org/10.1175/2010JPO4356.1

Blanke, B., Arhan, M., Madec, G., & Roche, S. (1999). Warm water paths in the equatorial Atlantic as diagnosed with a general circulation model. *Journal of Physical Oceanography*, 29(11), 2753–2768. https://doi.org/10.1175/1520-0485(1999)029<2753:WWPITE>2.0.CO;2

Bourlès, B., Araujo, M., McPhaden, M. J., Brandt, P., Foltz, G. R., Lumpkin, R., et al. (2019). PIRATA: A sustained observing system for tropical Atlantic climate research and forecasting. *Earth and Space Science*, 6(4), 577–616. https://doi.org/10.1029/2018EA000428

Bourlès, B., Gouriou, Y., & Chuchla, R. (1999). On the circulation in the upper layer of the western equatorial Atlantic. *Journal of Geophysical Research: Oceans*, 104(C9), 21151–21170.

Bourlès, B., Lumpkin, R., McPhaden, M. J., Hernandez, F., Nobre, P., Campos, E., et al. (2008). The PIRATA program: History, accomplishments, and future directions. *Bulletin of the American Meteorological Society*, 89(8), 1111–1126. https://doi.org/10.1175/2008BAMS2462.1

Bower, A., Lozier, S., Biastoch, A., Drouin, K., Foukal, N., Furey, H., et al. (2019). Lagrangian Views of the Pathways of the Atlantic Meridional Overturning Circulation. *Journal of Geophysical Research: Oceans*, 124(8), 5313–5335. https://doi.org/10.1029/2019jc015014

Brandt, P., Caniaux, G., Bourles, B., Lazar, A., Dengler, M., Funk, A., et al. (2011). Equatorial upper? Ocean dynamics and their interaction with the West African monsoon. *Atmospheric Science Letters*, 12(1), 24–30.

Brandt, P., Claus, M., Greatbatch, R. J., Kopte, R., Toole, J. M., Johns, W. E., & Böning, C. W. (2016). Annual and semiannual cycle of equatorial Atlantic circulation associated with basin-mode resonance. *Journal of Physical Oceanography*, 46(10), 3011–3029.

Brandt, P., Funk, A., Tantet, A., Johns, W. E., & Fischer, J. (2014). The Equatorial Undercurrent in the central Atlantic and its relation to tropical Atlantic variability. *Climate Dynamics*, 43(11), 2985–2997. https://doi.org/10.1007/s00382-014-2061-4

Brandt, P., Hahn, J., Schmidtko, S., Tuchen, F. P., Kopte, R., Kiko, R., et al. (2021). Atlantic Equatorial Undercurrent intensification counteracts warming-induced deoxygenation. *Nature Geoscience*, 14, 278–282. https://doi.org/10.1038/s41561-021-00716-1

Brandt, P., Hormann, V., Bourles, B., Fischer, J., Schott, F. A., Stramma, L., et al. (2008). Oxygen tongues and zonal currents in the equatorial Atlantic. *Journal of Geophysical Research: Oceans*, 113(C4), C04012. https://doi.org/10.1029/2007JC004435

Brandt, P., Schott, F. A., Provost, C., Kartavtseff, A., Hormann, V., Bourlès, B., & Fischer, J. (2006). Circulation in the central equatorial Atlantic: Mean and intraseasonal to seasonal variability. *Geophysical Research Letters*, 33(7). https://doi.org/10.1029/2005GL025498

Cabré, A., Pelegrí, J. L., & Vallès-Casanova, I. (2019). Subtropical-tropical transfer in the South Atlantic Ocean. *Journal of Geophysical Research: Oceans*, 124(7), 4820–4837. https://doi.org/10.1029/2019JC015160

Castellanos, P., Pelegrí, J. L., Campos, E. J., Rosell-Fieschi, M., & Gasser, M. (2015). Response of the surface tropical Atlantic Ocean to wind forcing. *Progress in Oceanography*, 134, 271–292. https://doi.org/10.1016/j.pocean.2015.02.005

Claret, M., Rodríguez-Marroyo, R., & Pelegrí, J. L. (2012). Salinity intrusion and convective mixing in the Atlantic Equatorial Undercurrent. *Scientia Marina*, 76(S1), 117–129. https://doi.org/10.3989/scimar.03611.19B

da Silveira, I. C. A., Miranda, L. B., & Brown, W. S. (1994). On the origins of the North Brazil Current. *Journal of Geophysical Research*, 99, 22501–22512. https://doi.org/10.1029/94JC01776

De La Fuente, P., Marrasé, C., Canepa, A., Álvarez-Salgado, X. A., Gasser, M., Fajar, N. M., et al. (2014). Does a general relationship exist between dissolved organic matter and microbial respiration?—The case of the dark equatorial Atlantic Ocean. *Deep-Sea Research I*, 89, 44–55.

Delandmeter, P., & van Sebille, E. (2019). The parcels v2.0 Lagrangian framework: New field interpolation schemes. *Geoscientific Model Development*, 12(8), 3571–3584. https://doi.org/10.5194/gmd-12-3571-2019

Döös, K., Nilsson, J., Nycander, J., Brodeau, L., & Ballarotta, M. (2012). The world ocean thermohaline circulation. *Journal of Physical Oceanography*, 42(9), 1445–1460. https://doi.org/10.1175/JPO-D-11-0163.1

Döös, K., Nycander, J., & Coward, A. C. (2008). Lagrangian decomposition of the Deacon cell. *Journal of Geophysical Research: Oceans*, 113(C7). https://doi.org/10.1029/2007JC004351

Egbert, G. D., Bennett, A. F., & Foreman, M. G. (1994). Topex/Poseidon tides estimated using a global inverse model. *Journal of Geophysical Research: Oceans*, 99(C12), 24821–24852. https://doi.org/10.1029/94JC01894

Foltz, G. R., Brandt, P., Richter, I., Rodríguez-Fonseca, B., Hernandez, F., Dengler, M., et al. (2019). The tropical Atlantic observing system. *Frontiers in Marine Science*, 6, 206.

Foltz, G. R., & McPhaden, M. J. (2010). Interaction between the Atlantic meridional and Niño modes. *Geophysical Research Letters*, 37(18). https://doi.org/10.1029/2010GL044001

Fraile-Nuez, E., & Hernández-Guerra, A. (2006). Wind-driven circulation for the eastern North Atlantic subtropical gyre from ARGO data. *Geophysical Research Letters*, 33(3). https://doi.org/10.1029/2005GL025122

Frajka-Williams, E., Beaulieu, C., & Duchez, A. (2017). Emerging negative Atlantic multidecadal oscillation index in spite of warm subtropics. *Scientific Reports*, 7, 11224. https://doi.org/10.1038/s41598-017-11046-x

Garric, G., Parent, L., Greiner, E., Drévillon, M., Hamon, M., Lellouche, J. M., et al. (2017). Performance and quality assessment of the global ocean eddy-permitting physical reanalysis GLORYS2V4. In *EGU General Assembly Conference Abstracts* (p. 18776).

Garzoli, S. L., Ffield, A., Johns, W. E., & Yao, Q. (2004). North Brazil Current retroflection and transports. *Journal of Geophysical Research: Oceans*, 109(C1). https://doi.org/10.1029/2003JC001775

Garzoli, S. L., & Katz, E. J. (1983). The forced annual reversal of the Atlantic North Equatorial Counter Current. *Journal of Physical Oceanography*, 13(11), 2082–2090. https://doi.org/10.1175/1520-0485(1983)013<2082:TFAROT>2.0.CO;2

Hammersley, J. (2013). *Monte Carlo methods*. Springer Science & Business Media.

Hazeleger, W., de Vries, P., & Friocourt, Y. (2003). Sources of the Equatorial Undercurrent in the Atlantic in a high-resolution ocean model. *Journal of Physical Oceanography*, 33(4), 677–693. https://doi.org/10.1175/1520-0485(2003)33<677:SOTEUI>2.0.CO;2

Hazeleger, W., & Drijfhout, S. (2006). Subtropical cells and meridional overturning circulation pathways in the tropical Atlantic. *Journal of Geophysical Research: Oceans*, 111(C3). https://doi.org/10.1029/2005JC002942

Hernández-Guerra, A., Pelegrí, J. L., Fraile-Nuez, E., Benítez-Barrios, V., Emelianov, M., Pérez-Hernández, M. D., & Vélez-Belchí, P. (2014). Meridional overturning transports at 7.5°N and 24.5°N in the Atlantic Ocean during 1992–93 and 2010–11. *Progress in Oceanography*, 128, 98–114.

Hormann, V., & Brandt, P. (2007). Atlantic Equatorial Undercurrent and associated cold tongue variability. *Journal of Geophysical Research: Oceans*, 112(C6). https://doi.org/10.1029/2006JC003931

Hormann, V., & Brandt, P. (2009). Upper equatorial Atlantic variability during 2002 and 2005 associated with equatorial Kelvin waves. *Journal of Geophysical Research: Oceans*, 114(C3). https://doi.org/10.1029/2008JC005101

Hormann, V., Lumpkin, R., & Foltz, G. R. (2012). Interannual North Equatorial Counter Current variability and its relation to tropical Atlantic climate modes. *Journal of Geophysical Research: Oceans*, *117*(C4).

Huang, B., Thorne, P. W., Banzon, V. F., Boyer, T., Chepurin, G., Lawrimore, J. H., et al. (2017). Extended Reconstructed Sea Surface Temperature version 5 (ERSSTv5), upgrades, validations, and intercomparisons. *Journal of Climate*, *30*(20), 8179–8205. https://doi.org/10.1175/JCLI-D-16-0836.1

Hüttl-Kabus, S., & Böning, C. W. (2008). Pathways and variability of the off-equatorial undercurrents in the Atlantic Ocean. *Journal of Geophysical Research: Oceans*, *113*(C10). https://doi.org/10.1029/2007JC004700

Illig, S., & Bachèlery, M. L. (2019). Propagation of subseasonal equatorially-forced coastal trapped waves down to the Benguela upwelling system. *Scientific Reports*, *9*(1), 1–10. https://doi.org/10.1038/s41598-019-41847-1

Illig, S., Dewitte, B., Ayoub, N., Du Penhoat, Y., Reverdin, G., De Mey, P., et al. (2004). Interannual long equatorial waves in the tropical Atlantic from a high-resolution ocean general circulation model experiment in 1981–2000. *Journal of Geophysical Research: Oceans*, *109*(C2). https://doi.org/10.1029/2003JC001771

Johns, W. E., Brandt, P., Bourlès, B., Tantet, A., Papapostolou, A., & Houk, A. (2014). Zonal structure and seasonal variability of the Atlantic Equatorial Undercurrent. *Climate Dynamics*, *43*(11), 3047–3069. https://doi.org/10.1007/s00382-014-2136-2

Jouanno, J., Marin, F., Du Penhoat, Y., Sheinbaum, J., & Molines, J.-M. (2011). Seasonal heat balance in the upper 100 m of the equatorial Atlantic Ocean. *Journal of Geophysical Research: Oceans*, *116*(C9). https://doi.org/10.1029/2010JC006912

Katz, E. J. (1987). Seasonal response of the sea surface to the wind in the equatorial Atlantic. *Journal of Geophysical Research: Oceans*, *92*(C2), 1885–1893. https://doi.org/10.1029/JC092iC02p01885

Kolodziejczyk, N., Bourlès, B., Marin, F., Grelet, J., & Chuchla, R. (2009). Seasonal variability of the Equatorial Undercurrent at 10°W was inferred from recent in situ observations. *Journal of Geophysical Research: Oceans*, *114*(C6), C06014. https://doi.org/10.1029/2008JC004976

Kolodziejczyk, N., Marin, F., Bourlès, B., Gouriou, Y., & Berger, H. (2014). Seasonal variability of the Equatorial Undercurrent termination and associated salinity maximum in the Gulf of Guinea. *Climate Dynamics*, *43*(11), 3025–3046. https://doi.org/10.1007/s00382-014-2107-7

Lübbecke, J. F., Böning, C. W., Keenlyside, N. S., & Xie, S. P. (2010). On the connection between Benguela and equatorial Atlantic Niños and the role of the South Atlantic anticyclone. *Journal of Geophysical Research: Oceans*, *115*(C9), C09015.

Lübbecke, J. F., Rodríguez-Fonseca, B., Richter, I., Martín-Rey, M., Losada, T., Polo, I., & Keenlyside, N. S. (2018). Equatorial Atlantic variability: Modes, mechanisms, and global teleconnections. *Wiley Interdisciplinary Reviews: Climate Change*, *9*(4), e527. https://doi.org/10.1002/wcc.527

Lumpkin, R., & Garzoli, S. L. (2005). Near-surface circulation in the tropical Atlantic Ocean. *Deep Sea Research Part I: Oceanographic Research Papers*, *52*(3), 495–518. https://doi.org/10.1016/j.dsr.2004.09.001

Madec, G. (2008). *Nemo ocean engine*. Retrieved from www.nemo-ocean.eu

Martín-Rey, M., & Lazar, A. (2019). Is the boreal spring tropical Atlantic variability a precursor of the equatorial mode? *Climate Dynamics*, *53*(3), 2339–2353.

Martín-Rey, M., Polo, I., Rodríguez-Fonseca, B., Lazar, A., & Losada, T. (2019). Ocean dynamics shapes the structure and timing of Atlantic equatorial modes. *Journal of Geophysical Research: Oceans*, *124*(11), 7529–7544.

Martín-Rey, M., Polo, I., Rodríguez-Fonseca, B., Losada, T., & Lazar, A. (2018). Is there evidence of changes in tropical Atlantic variability modes under AMO phases in the observational record? *Journal of Climate*, *31*(2), 515–536. https://doi.org/10.1175/JCLI-D-16-0459.1

McCreary, J. P., Jr., & Lu, P. (1994). Interaction between the subtropical and equatorial ocean circulations: The subtropical cell. *Journal of Physical Oceanography*, *24*(2), 466–497. https://doi.org/10.1175/1520-0485(1994)024<0466:IBTSAE>2.0.CO;2

Mémery, L., Arhan, M., Alvarez-Salgado, X. A., Messias, M.-J., Mercier, H., Castro, C. G., & Rios, A. F. (2000). The water masses along the western boundary of the South and equatorial Atlantic. *Progress in Oceanography*, *47*(1), 69–98. https://doi.org/10.1016/S0079-6611(00)00032-X

Ménesguen, C., Delpech, A., Marin, F., Cravatte, S., Schopp, R., & Morel, Y. (2019). Observations and mechanisms for the formation of deep equatorial and tropical circulation. *Earth and Space Science*, *6*, 370–386. https://doi.org/10.1029/2018EA000438

Mercier, H., Arhan, M., & Lutjeharms, J. R. (2003). Upper-layer circulation in the eastern equatorial and South Atlantic Ocean in January–March 1995. *Deep-Sea Research Part I: Oceanographic Research Papers*, *50*(7), 863–887. https://doi.org/10.1016/S0967-0637(03)00071-2

Metcalf, W., & Stalcup, M. C. (1967). Origin of the Atlantic Equatorial Undercurrent. *Journal of Geophysical Research*, *72*(20), 4959–4975. https://doi.org/10.1029/JZ072i020p04959

Metcalf, W., Voorhis, A., & Stalcup, M. (1962). The Atlantic Equatorial Undercurrent. *Journal of Geophysical Research*, *67*(6), 2499–2508. https://doi.org/10.1029/JZ067i006p02499

Mignac, D., Ferreira, D., & Haines, K. (2018). South Atlantic meridional transports from nemo-based simulations and reanalyses. *Ocean Science*, *14*(1), 53–68. https://doi.org/10.5194/os-14-53-2018

Nobre, P., & Shukla, J. (1996). Variations of sea surface temperature, wind stress, and rainfall over the tropical Atlantic and South America. *Journal of Climate*, *9*(10), 2464–2479.

Pelegrí, J. L., Vallès-Casanova, I., Benítez-Barrios, V. M., Castellanos, P., Claret, M., De la Fuente, P., et al. (2022). Hydrographic and velocity data during Leg 1 of the R/V Hespérides MOC2 cruise, 7-18 April 2010, western equatorial Atlantic. [Dataset]. . https://doi.org/10.5281/zenodo.6359412

Peña-Izquierdo, J., van Sebille, E., Pelegrí, J. L., Sprintall, J., Mason, E., Llanillo, P. J., & Machín, F. (2015). Water mass pathways to the North Atlantic oxygen minimum zone. *Journal of Geophysical Research: Oceans*, *120*(5), 3350–3372. https://doi.org/10.1002/2014JC010557

Perez, R. C., Hormann, V., Lumpkin, R., Brandt, P., Johns, W. E., Hernandez, F., et al. (2014). Mean meridional currents in the central and eastern equatorial Atlantic. *Climate Dynamics*, *43*(11), 2943–2962.

Perez, R. C., Lumpkin, R., Johns, W. E., Foltz, G. R., & Hormann, V. (2012). Interannual variations of Atlantic tropical instability waves. *Journal of Geophysical Research: Oceans*, *117*(C3). https://doi.org/10.1029/2011JC007584

Philander, S., & Pacanowski, R. (1986). A model of the seasonal cycle in the tropical Atlantic ocean. *Journal of Geophysical Research: Oceans*, *91*(C12), 14192–14206. https://doi.org/10.1029/JC091iC12p14192

Polo, I., Lazar, A., Rodríguez-Fonseca, B., & Arnault, S. (2008). Oceanic Kelvin waves and tropical Atlantic intraseasonal variability: 1. Kelvin wave characterization. *Journal of Geophysical Research: Oceans*, *113*(C7). https://doi.org/10.1029/2007JC004495

Polonsky, A. B., & Artamonov, Y. V. (1997). North Equatorial Counter Current in the tropical Atlantic: Multi-jet structure and seasonal variability. *Deutsche Hydrografische Zeitschrift*, *49*(4), 477–495. https://doi.org/10.1007/BF02764342

Richter, I., Behera, S. K., Masumoto, Y., Taguchi, B., Sasaki, H., & Yamagata, T. (2013). Multiple causes of interannual sea surface temperature variability in the equatorial Atlantic Ocean. *Nature Geoscience*, *6*(1), 43–47. https://doi.org/10.1038/ngeo1660

Richter, I., & Tokinaga, H. (2020). An overview of the performance of CMIP6 models in the tropical Atlantic: Mean state, variability, and remote impacts. *Climate Dynamics*, *55*(9), 2579–2601.

Richter, I., & Xie, S. P. (2008). On the origin of equatorial Atlantic biases in coupled general circulation models. *Climate Dynamics*, *31*(5), 587–598.

Richter, I., Xie, S. P., Wittenberg, A. T., & Masumoto, Y. (2012). Tropical Atlantic biases and their relation to surface wind stress and terrestrial precipitation. *Climate Dynamics*, *38*(5), 985–1001.

Ríos, A. F., Pérez, F. F., Pelegrí, J. L., & Fajar, N. M. (2012). *Carbon Data Obtained during the R/V Hesperides Cruise in the Atlantic Ocean on CLIVAR Repeat Hydrography Section A06 (5 April to 16 May, 2010)*. Carbon Dioxide Information Analysis Center, Oak Ridge National Laboratory, US Department of Energy. https://doi.org/10.3334/CDIAC/OTG.CLIVAR_A06_2010

Rosell-Fieschi, M., Pelegrí, J. L., & Gourrion, J. (2015). Zonal jets in the equatorial Atlantic Ocean. *Progress in Oceanography*, *130*, 1–18. https://doi.org/10.1016/j.pocean.2014.08.008

San Antolín Plaza, M. A., Pelegrí, J. L., Machin, F. J., & Benítez Barrios, V. (2012). Inter-decadal changes in stratification and double diffusion in a transatlantic section along 7.5°N. *Scientia Marina*, *76*(S1), 189–207. https://doi.org/10.3989/scimar.03616.19G

Schlundt, M., Brandt, P., Dengler, M., Hummels, R., Fischer, T., Bumke, K., et al. (2014). Mixed layer heat and salinity budgets during the onset of the 2011 Atlantic cold tongue. *Journal of Geophysical Research: Oceans*, *119*(11), 7882–7910. https://doi.org/10.1002/2014JC010021

Schott, F. A., & Böning, C. W. (1991). The WOCE model in the western equatorial Atlantic: Upper layer circulation. *Journal of Geophysical Research: Oceans*, *96*(C4), 6993–7004. https://doi.org/10.1029/90jc02683

Schott, F. A., Dengler, M., Brandt, P., Affler, K., Fischer, J., Bourles, B., et al. (2003). The zonal currents and transports at 35°W in the tropical Atlantic. *Geophysical Research Letters*, *30*(7), 1349. https://doi.org/10.1029/2002GL016849

Schott, F. A., Dengler, M., Zantopp, R., Stramma, L., Fischer, J., & Brandt, P. (2005). The shallow and deep western boundary circulation of the South Atlantic at 5°–11°S. *Journal of Physical Oceanography*, *35*(11), 2031–2053. https://doi.org/10.1175/JPO2813.1

Schott, F. A., Mccreary, J. P., & Johnson, G. C. (2004). Shallow overturning circulations of the tropical-subtropical oceans. *Earth Climate: The Ocean-Atmosphere Interaction*, *147*, 261–304. https://doi.org/10.1029/147GM15

Stramma, L., Fischer, J., & Reppin, J. (1995). The North Brazil undercurrent. *Deep-Sea Research Part I: Oceanographic Research Papers*, *42*(5), 773–795.

Stramma, L., & Schott, F. (1999). The mean flow field of the tropical Atlantic ocean. *Deep-Sea Research Part II: Topical Studies in Oceanography*, *46*(1–2), 279–303. https://doi.org/10.1016/S0967-0645(98)00109-X

Tamsitt, V., Abernathey, R. P., Mazloff, M. R., Wang, J., & Talley, L. D. (2018). Transformation of deep water masses along Lagrangian upwelling pathways in the Southern Ocean. *Journal of Geophysical Research: Oceans*, *123*(3), 1994–2017. https://doi.org/10.1002/2017JC013409

Tuchen, F. P., Brandt, P., Lübbecke, J. F., & Hummels, R. (2022). Transports and pathways of the tropical AMOC return flow from Argo data and shipboard velocity measurements. *Journal of Geophysical Research: Oceans*, *127*, e2021JC018115. https://doi.org/10.1029/2021JC018115

Tuchen, F. P., Lübbecke, J. F., Brandt, P., & Fu, Y. (2020). Observed transport variability of the Atlantic subtropical cells and their connection to tropical sea surface temperature variability. *Journal of Geophysical Research: Oceans*, *125*(12), e2020JC016592. https://doi.org/10.1029/2020JC016592

Tuchen, F. P., Lübbecke, J. F., Schmidtko, S., Hummels, R., & Böning, C. W. (2019). The Atlantic subtropical cells inferred from observations. *Journal of Geophysical Research: Oceans*, *124*(11), 7591–7605.

Urbano, D., De Almeida, R., & Nobre, P. (2008). Equatorial Undercurrent and North Equatorial Counter Current at 38°W: A new perspective from direct velocity data. *Journal of Geophysical Research: Oceans*, *113*(C4). https://doi.org/10.1029/2007JC004215

Vallès-Casanova, I., Lee, S.-K., Foltz, G. R., & Pelegrí, J. L. (2020). On the spatiotemporal diversity of Atlantic Niño and associated rainfall variability over West Africa and South America. *Geophysical Research Letters*, *47*(8), e2020GL087108. https://doi.org/10.1029/2020GL087108

Van Sebille, E., Sprintall, J., Schwarzkopf, F. U., Sen Gupta, A., Santoso, A., England, M. H., et al. (2014). Pacific-to-Indian ocean connectivity: Tasman leakage, Indonesian throughflow, and the role of ENSO. *Journal of Geophysical Research: Oceans*, *119*(2), 1365–1382. https://doi.org/10.1002/2013JC009525

Visbeck, M. (2002). Deep velocity profiling using lowered acoustic Doppler current profilers: Bottom track and inverse solutions. *Journal of Atmospheric and Oceanic Technology*, *19*(5), 794–807. https://doi.org/10.1175/1520-0426(2002)019<0794:DVPULA>2.0.CO;2

Von Schuckmann, K., Brandt, P., & Eden, C. (2008). Generation of tropical instability waves in the Atlantic Ocean. *Journal of Geophysical Research: Oceans*, *113*(C8). https://doi.org/10.1029/2007JC004712

Von Schuckmann, K., Le Traon, P.-Y., Alvarez-Fanjul, E., Axell, L., Balmaseda, M., Breivik, L.-A., et al. (2017). The Copernicus marine environment monitoring service ocean state report. *Journal of Operational Oceanography*, *9*(sup 2), s235–s320. https://doi.org/10.1080/1755876X.2016.1273446

Wang, C., & Zhang, L. (2013). Multidecadal ocean temperature and salinity variability in the tropical North Atlantic: Linking with the AMO, AMOC, and subtropical cell. *Journal of Climate*, *26*(16), 6137–6162.

White, R. (2015). Using multiple passive tracers to identify the importance of the North Brazil Undercurrent for Atlantic cold tongue variability. *Quarterly Journal of the Royal Meteorological Society*, *141*(692), 2505–2517. https://doi.org/10.1002/qj.2536

Zebiak, S. E. (1993). Air-sea interaction in the equatorial Atlantic region. *Journal of Climate*, *6*(8), 1567–1586. https://doi.org/10.1175/1520-0442(1993)006<1567:AIITEA>2.0.CO;2

Zhang, D., McPhaden, M. J., & Johns, W. E. (2003). Observational evidence for flow between the subtropical and tropical Atlantic: The Atlantic subtropical cells. *Journal of Physical Oceanography*, *33*(8), 1783–1797.